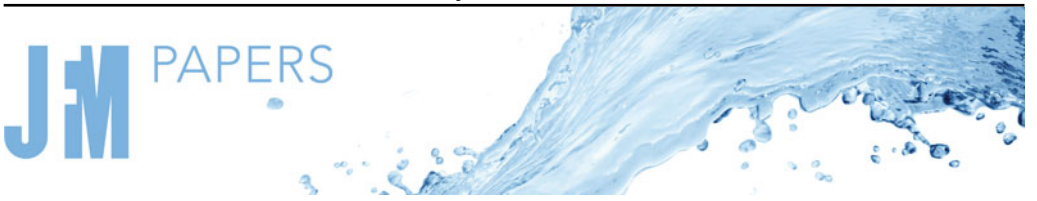
J. Fluid Mech. (2025), *vol.* 1025, A5, doi:10.1017/jfm.2025.10871



On the stability and dynamics of flows past bubble-shaped rigid bluff bodies

Ragavendiran Muniyammal[1], **Shyam Sunder Gopalakrishnan**[2], **Sanjay Kumar**[1] **and Alakesh Chandra Mandal**[1]

[1]Department of Aerospace Engineering, Indian Institute of Technology Kanpur, Kanpur 208016, India

[2]Department of Mechanical Engineering, Indian Institute of Technology Kanpur, Kanpur 208016, India

Corresponding authors: Ragavendiran Muniyammal, ragavcandela@gmail.com; Shyam Sunder Gopalakrishnan, shyamsg@iitk.ac.in; Sanjay Kumar, skmr@iitk.ac.in; Alakesh Chandra Mandal, alakeshm@iitk.ac.in

(Received 26 December 2024; revised 14 August 2025; accepted 6 October 2025)

The stability and dynamics of flows past axisymmetric bubble-shaped rigid bluff bodies have been numerically and experimentally investigated. Motivated by the shapes of bubbles rising in quiescent liquids the bluff bodies were modelled as spherical and elliptical caps. The geometries are characterised by their aspect ratio, χ, defined as the ratio of the height of the bubble to the base radius, which is varied from 0.2 to 2.0. Linear stability analyses were carried out on axisymmetric base flow fields subject to three-dimensional perturbations. As observed in earlier studies on bluff-body wakes, the primary bifurcation is stationary, followed by an oscillatory secondary bifurcation, with the leading global mode corresponding to azimuthal wavenumber $m = 1$. The domain of stability is found to increase with aspect ratio for both of the geometries considered in the present study. The critical Reynolds number corresponding to the primary bifurcation is found to be independent of the aspect ratio when re-scaled using the extent of the recirculation region and the maximum of the reverse-flow velocity as the length and velocity scales, respectively. The wake flow features were characterised experimentally using laser-induced fluorescence and particle-image-velocimetry techniques. It is observed that the flow has a planar symmetry following the primary bifurcation, which is retained beyond the secondary bifurcation. The experimentally measured wavelengths and frequencies are in excellent agreement with the results obtained from global stability analyses. These observations were further corroborated using direct numerical simulations of the three-dimensional flow field. The critical Reynolds numbers corresponding to both primary and secondary bifurcations, and the dominant modes obtained using proper orthogonal decomposition of the experimentally measured velocity fields, are found to agree well with the global mode shapes and numerically computed flow fields.

https://doi.org/10.1017/jfm.2025.10871 Published online by Cambridge University Press

© The Author(s), 2025. Published by Cambridge University Press.

Key words: wakes, vortex shedding, absolute/convective instability

1. Introduction

The global dynamics of flows past axisymmetric bluff bodies at moderate Reynolds numbers is now fairly well established, both experimentally and numerically. In this regard, previous investigations have been mainly carried out for the wake flows around a sphere (Taneda 1956; Magarvey & Bishop 1961*b*; Roos & Willmarth 1971; Nakamura 1976; Natarajan & Acrivos 1993; Johnson & Patel 1999; Ormières & Provansal 1999; Ghidersa & Dušek 2000; Gumowski *et al.* 2008; Pier 2008), bullet-shaped bodies (Sanmiguel-Rojas *et al.* 2009, 2011; Bohorquez *et al.* 2011), discs (Fabre, Auguste & Magnaudet 2008; Meliga, Chomaz & Sipp 2009; Szaltys *et al.* 2012; Bobinski, Goujon-Durand & Wesfreid 2014), spheroids (Mittal 1999; Chrust, Bouchet & Dušek 2010) and hemispheres (Kim & Choi 2003) (for a comprehensive review please refer to Ern *et al.* 2012). These studies have revealed that the sequence of transitions which occur with increasing values of the Reynolds number differs in a subtle manner among these bluff bodies. The first bifurcation is a stationary one associated with a pair of counter-rotating azimuthal modes for azimuthal wavenumber $m = \pm 1$. As the Reynolds number increases, a second transition/bifurcation occurs, leading to the formation of a hairpin-shaped vortex structure from double-threaded vortex structures. This second transition is known as the secondary bifurcation, which is unsteady. In the case of spheres and bullet-shaped bluff bodies, the wake is planar symmetric, which is conserved in the unsteady time-periodic regime up to a certain Reynolds number. However, in the wake of a hemisphere and of thin discs, the secondary oscillatory bifurcation does not preserve the symmetry plane (Ern *et al.* 2012). Furthermore, the errors in the predictions made by the global linear stability analysis performed on axisymmetric base flows with non-axisymmetric ones vary greatly among these geometries. For instance, in the case of spheres and thin discs, the critical Reynolds number at which the transition from a steady non-axisymmetric wake to periodic vortex shedding occurs is in remarkable agreement between both the approaches whereas, for bullet-shaped bodies, the error is substantially higher (Bohorquez *et al.* 2011). This can be attributed to the relative difference of the critical Reynolds numbers corresponding to the primary and secondary bifurcations, $\Delta = (Re_{c2} - Re_{c1})/Re_{c1}$ (Fabre *et al.* 2008; Bohorquez *et al.* 2011); here, Re_{c1} and Re_{c2} denote the critical Reynolds number corresponding to the primary and secondary bifurcations, respectively. If Δ is much less than 1, the global stability analysis considering the axisymmetric steady base flow can closely predict Re_{c2} (Bohorquez *et al.* 2011). This condition closely holds good for thin discs, a sphere, and a bullet-shaped body with unit aspect ratio, but fails to do so for blunt-shaped slender bodies, and ellipsoids with large aspect ratios (see figure 14 in Bohorquez *et al.* 2011, for an example). The present study aims to address the above aspect by studying the stability and dynamics of flows past bubble-shaped bluff-bodies, modelled as spherical and elliptical caps, both numerically and experimentally.

The transition scenarios arising in bluff-body wakes were first qualitatively revealed by the experimental studies carried out on immiscible drops (Magarvey & Bishop 1961*a*, *b*) and liquid-filled spheres (Magarvey & MacLatchy 1965) falling in water. By choosing density ratios between the fluids such that the bodies underwent only tiny displacements, they were able to qualitatively describe the first two bifurcation states arising in the flow past a rigid sphere. In the case of falling drops, the presence of surface-active impurities at the liquid–liquid interface ensured that they stayed in a semi-rigid spherical shape, thereby allowing a qualitative comparison with flows past rigid bodies. These were further

https://doi.org/10.1017/jfm.2025.10871 Published online by Cambridge University Press

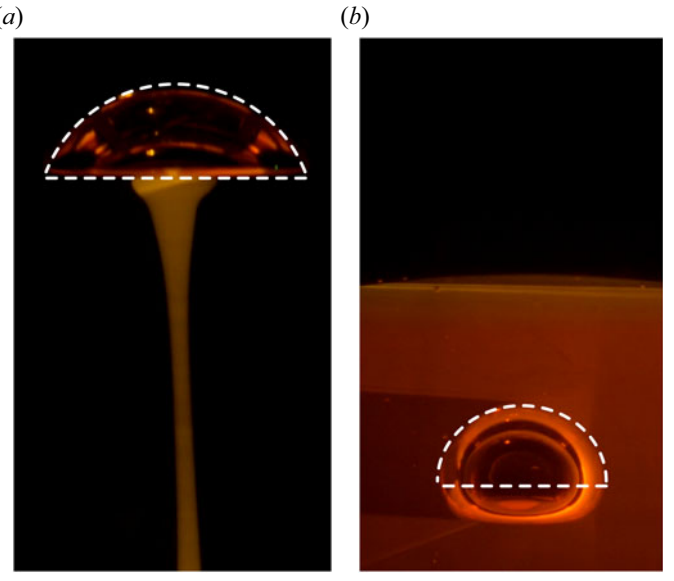


Figure 1. Present shapes of bluff bodies inspired from our previous work on rising bubbles which are available as APSDFD2020 video (Muniyammal, Mandal & Kumar 2020). These are modelled here as (*a*) spherical and (*b*) elliptical caps. The dotted lines correspond to (*a*) $\chi = 0.6$ and (*b*) $\chi = 0.8$.

extended and corroborated by Nakamura (1976). Similar qualitative comparisons have also been made from studies carried out on freely rising axisymmetric bodies such as bubbles and spheroids (Magnaudet & Mougin 2007; Ern *et al.* 2012). The bubble dynamics is indeed more complicated than that of solid bodies (Fernandes *et al.* 2007; Cano-Lozano *et al.* 2016; Bonnefis *et al.* 2024). Using both experimental and numerical methods, it has been established that the shape fluctuations do not play a significant role in the regime of path oscillations of bubbles rising in clean water (Ellingsen & Risso 2001; Mougin & Magnaudet 2001). The aspect ratio of the bubble remains the same after the initial transients, with the bubble attaining a terminal shape and velocity. Studying the wake of fixed axisymmetric bodies is a necessary step towards understanding the characteristics observed in the aforementioned systems (Ern *et al.* 2012). Figure 1 shows the experimentally observed axisymmetric bubble-shape configurations considered in the present work, which are modelled as spherical and elliptical caps. The geometries are characterised by the aspect ratio χ, which is defined as the ratio of the height of the bubble (measured in the direction parallel to the revolution axis) and the radius of its base. The aspect ratio is varied in the range $0.2 \leqslant \chi \leqslant 2$, which qualitatively corresponds to the different shapes observed for a bubble rising in quiescent fluid. To our knowledge, such bubble-shaped solid bodies of intermediate shape have not been studied yet, and it is expected that their wakes will also present specific features, which are worth investigating experimentally and numerically.

It is by now well established that the wakes of axisymmetric bluff bodies are characterised by a region of absolute instability, the spatial extent of which, interestingly, closely follows the toroidal recirculating region downstream of the bluff body (Chomaz 2005; Pier 2008; Meliga *et al.* 2009). It has been shown that the recirculation zone could be viewed as an effective wave maker, with the pocket of absolute instability within it fixing the global shedding frequency (Monkewitz 1988; Pier 2008; Meliga *et al.* 2009). Furthermore, as the onset of instability is related to the amount of vorticity generated at the body's surface, a relevant velocity scale to characterise this downstream vortex is the

https://doi.org/10.1017/jfm.2025.10871 Published online by Cambridge University Press

maximum reverse-flow velocity on its axis (Fernandes *et al.* 2007; Magnaudet & Mougin 2007). By defining a modified Reynolds number based on the recirculation length, L_r, and the maximum of the reverse-flow velocity, U_{rev}, Fernandes *et al.* (2007) have shown that the dimensional amplitudes and frequencies observed in freely rising axisymmetric bodies are independent of the body shape. Although the flow structures observed in plane wakes past two-dimensional symmetric bluff bodies are qualitatively different, it has been shown recently that L_r and U_{rev} are indeed the relevant length and velocity scales to describe the primary instability (Chiarini, Quadrio & Auteri 2022). The predicted scaling law has been shown to be robust and holds for planar wakes corresponding to differently shaped geometries. The choice of the velocity scale was attributed to the fact that the spatial location corresponding to U_{rev} is the region associated with the largest axial shear (Hammond & Redekopp 1997). As reverse flow enhances the growth of disturbances travelling upstream of the absolutely unstable region (Monkewitz 1988), the choice of L_r and U_{rev} as the relevant scales indeed seem pertinent. Indeed, as the vortex shedding from axisymmetric bodies is different from planar bodies as it is sensitive to the shape of the bluff body and the nature of separation on the body (Monkewitz 1988), it is worthwhile examining the validity of the existing scaling laws. We show that the critical Reynolds number corresponding to the primary bifurcation remains independent of the aspect ratio when scaled by L_r and U_{rev}.

The main objective of the present work is to examine the flow regimes taking place in the laminar wake of axisymmetric bluff bodies, modelled as spherical and elliptical caps. By combining flow visualisations and particle-image-velocimetry techniques, and global stability analyses, we investigate the following: (*a*) whether the aspect ratios for which the critical Reynolds numbers predicted using axisymmetric base flow fields are in agreement with the experimental observations made using dye visualisations and particle-image-velocimetry techniques; (*b*) whether the reported scaling laws on planar wakes past bluff bodies (Chiarini *et al.* 2022), based on maximum reverse-flow velocity and the recirculation length, hold for flows past axisymmetric geometries; (*c*) and we qualitatively provide insight into the symmetry preserving/breaking nature of flows past axisymmetric bodies using dye visualisations and particle image velocimetry. The observed findings are in excellent agreement with the available literature on flow past a hemisphere ($\chi = 1$) (Kim & Choi 2003; Jiménez-González *et al.* 2019), and with the wake of a blunt-shaped cylindrical body with a rounded ellipsoidal nose ($\chi = 2$) (Bohorquez *et al.* 2011).

To this end, the paper is organised as follows. The geometrical configurations, the numerical methods and the experimental techniques used in the present study are described in § 2. The base flow characteristics and the results from the global linear stability analyses for geometries with varying aspect ratios are discussed in detail in § 3. Comparisons of the numerically obtained results with experimental observations using flow visualisation and particle-image-velocimetry techniques are presented in § 4. The article ends with concluding remarks in § 5.

2. Methodology

2.1. *Geometry*

The geometrical configurations considered in the present study are based on the shapes observed as a bubble rises through a quiescent liquid (see figure 1). The shape of the rising bubble can vary greatly depending on the solutal composition of the surrounding liquid, or indeed as it passes through a liquid–liquid interface (figure 1*b*). The bubble shape is modelled as an elliptical cap, and as a spherical cap with a flat circular base. These are shown in figure 2 in panels (*a*) and (*b*), respectively. The shapes are characterised by the diameter of

https://doi.org/10.1017/jfm.2025.10871 Published online by Cambridge University Press

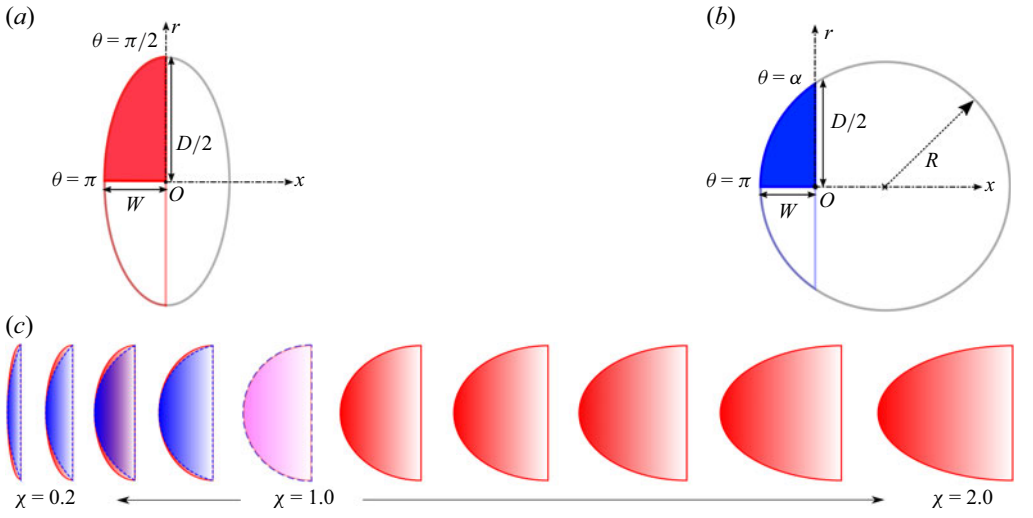


Figure 2. Schematic of the geometrical configurations. Bubble-shaped bluff bodies modelled as an (*a*) elliptical cap, and (*b*) as a spherical cap. (*c*) Comparison of the two different configurations with increasing aspect ratio, with the spherical cap denoted by dashed blue lines, and the elliptical cap by solid red lines. The spherical cap shapes were considered within the range of aspect ratios $0.2 \leqslant \chi \leqslant 1$ whereas the bubble surface modelled as an elliptical cap extends up to $\chi = 2$. The case of a hemisphere corresponds to $\chi = 1$.

the circular base D, and by the width (or height) of the bubble W. The varying shapes can be geometrically characterised by the aspect ratio $\chi = W/(D/2)$, as shown in figure 2(*c*).

From the axisymmetry of the geometrical configuration a cylindrical coordinate system has been used for global linear stability analysis investigation with r, θ and x denoting radial, azimuthal and axial coordinates respectively. The x-axis is aligned with the free-stream velocity, with the origin at the centre of the circular base, as shown in figure 2. The bubble surfaces modelled as elliptical caps are defined by the following parametric equations:

$$x = W\cos\theta, \qquad r = \frac{D}{2}\sin\theta, \tag{2.1}$$

with θ varying from π to $\pi/2$. The spherical cap on the other hand is defined based on the sphere of which it forms a part, as

$$x = (R - W) + R\cos\theta, \qquad r = R\sin\theta, \tag{2.2}$$

with R being the radius of the sphere, and θ denoting an angle varying between π and the desired angle α. These are given by

$$R = \frac{(D^2/4 + W^2)}{2W}, \quad \tan\alpha = \frac{D/2}{(R - W)}. \tag{2.3}$$

It is to be noted that the bubble shape modelled as a spherical cap corresponds to a part of a sphere, and beyond $\chi > 1$ the maximum diameter exceeds the base diameter D. To this end the aspect ratios were varied within the range $0.2 \leqslant \chi \leqslant 1$ for the spherical cap, and $0.2 \leqslant \chi \leqslant 2$ for the elliptical cap.

2.2. *Governing equations*

The governing equations are the Navier–Stokes equations. Here, we consider these equations for an incompressible axisymmetric flow in the cylindrical coordinate system (x, r, θ) for a fluid with density ρ and dynamic viscosity μ. The characteristic length, time,

https://doi.org/10.1017/jfm.2025.10871 Published online by Cambridge University Press

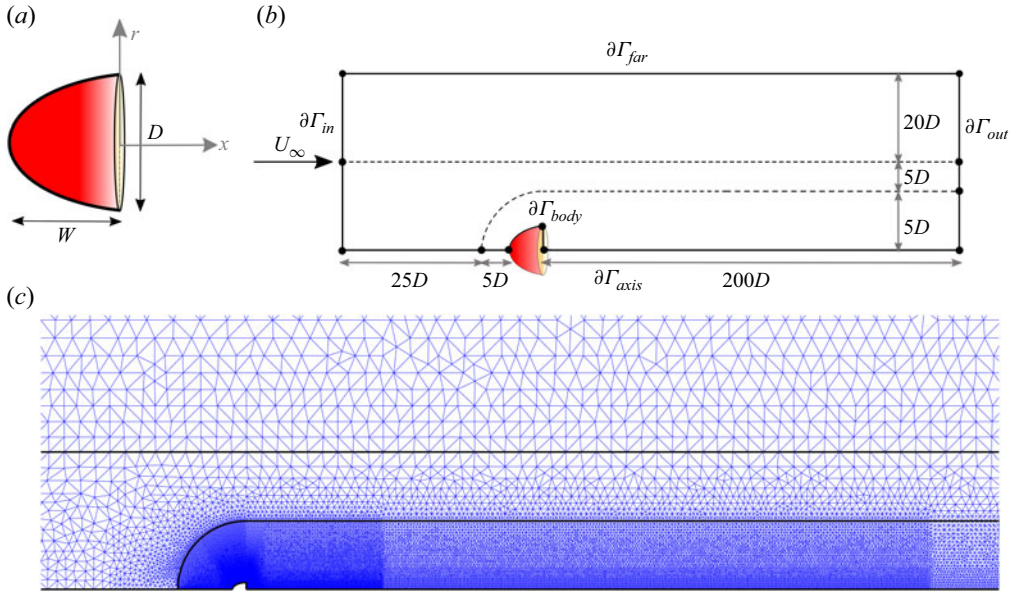


Figure 3. Sketch of the body and the computational domain in the x, r, θ coordinate system. The axial direction x is aligned with the free-stream velocity U_∞, with the origin at the centre of the circular base of diameter D (a). The domain boundaries are denoted as $\partial\Gamma_{in}$ (inlet), $\partial\Gamma_{out}$ (outlet), Γ_{far} (upper) and $\partial\Gamma_{body}$ (body) (b). The mesh in the computational domain is shown in (c).

velocity and pressure scales are considered as D, D/U_∞, U_∞ and ρU_∞^2, respectively. With these scales, the non-dimensional forms of the governing equations are given as follows:

$$\partial_t \boldsymbol{u} + (\boldsymbol{u}\cdot\nabla)\boldsymbol{u} = -\nabla p + \frac{1}{Re}\nabla^2\boldsymbol{u}, \tag{2.4a}$$

$$\nabla\cdot\boldsymbol{u} = 0. \tag{2.4b}$$

Here, $Re = \rho U_\infty D/\mu$ is the Reynolds number, $\boldsymbol{u}$ (u_x, u_r, u_θ) is velocity vector and p is the pressure. These equations are solved in the axisymmetric coordinate system keeping the origin at the centre of the base, as schematically shown in figure 3(a). The computational domain, Ω, is shown in figure 3(b). We used the following boundary conditions to solve the above equations. At the inlet boundary ($\partial\Gamma_{in}$), a uniform axial velocity $\boldsymbol{u} = (U_\infty, 0, 0)$ was prescribed. A no-slip condition ($\boldsymbol{u} = 0$) was enforced on the model surface ($\partial\Gamma_{body}$). A no-stress condition was imposed at the outlet ($\partial\Gamma_{out}$), while a free-slip condition is applied at the far-field boundary ($\partial\Gamma_{far}$). The resulting velocity field from this simulation is used as the initial guess for the computation of the base flow. The base flow field ($\overline{u}_x, \overline{u}_r, \overline{u}_\theta$ and $\overline{p}$) was calculated using the steady equations,

$$(\overline{\boldsymbol{u}}.\nabla)\overline{\boldsymbol{u}} = -\nabla\bar{p} + \frac{1}{Re}\nabla^2\overline{\boldsymbol{u}}, \tag{2.5a}$$

$$\nabla.\overline{\boldsymbol{u}} = 0, \tag{2.5b}$$

with similar boundary conditions discussed above for (2.4).

The stability analysis of the above base flow was performed by superimposing an infinitesimal(ϵ) three-dimensional perturbation $(\boldsymbol{u}', p')$ on the base flow field, i.e. $(u_x, u_r, u_\theta, p) = (\overline{u}_x, \overline{u}_r, \overline{u}_\theta, \overline{p}) + \epsilon(u'_x, u'_r, u'_\theta, p')$. The evolution of these perturbations is governed by the linearised Navier–Stokes equations

https://doi.org/10.1017/jfm.2025.10871 Published online by Cambridge University Press

$$\frac{\partial \boldsymbol{u}'}{\partial t} + (\overline{\boldsymbol{u}}.\boldsymbol{\nabla})\boldsymbol{u}' + (\boldsymbol{u}'.\boldsymbol{\nabla})\overline{\boldsymbol{u}} = -\boldsymbol{\nabla} p' + \frac{1}{Re}\nabla^2 \boldsymbol{u}', \tag{2.6a}$$

$$\boldsymbol{\nabla}.\boldsymbol{u}' = 0. \tag{2.6b}$$

These equations were converted to an eigenvalue problem by considering the following normal-mode form of the perturbations:

$$[\boldsymbol{u}',\ p'](r, \theta, x, t) = [\hat{u}_r, \hat{u}_\theta, \hat{u}_x, \hat{p}](r, x) e^{im\theta + \lambda t} + \text{c.c}, \tag{2.7}$$

where c.c denotes complex conjugate, $m \in \mathbb{R}$ is the azimuthal mode number and $\lambda = \sigma + i\omega$ is the complex eigenfrequency. The growth rate and the circular frequency are given by σ and ω, respectively. The perturbations are stationary when $\omega = 0$ and oscillatory when $\omega \neq 0$.

Substituting the normal-mode form (2.7) in the linearised Navier–Stokes equations ((2.6*a*) and (2.6*b*)), one can get a generalised eigenvalue problem of the form

$$\boldsymbol{A}\hat{\boldsymbol{u}} + \lambda \boldsymbol{B}\hat{\boldsymbol{u}} = 0, \tag{2.8}$$

where $\hat{\boldsymbol{u}} = [\hat{u}_x, \hat{u}_r, \hat{u}_\theta, \hat{p}]$ is a vector consisting of the shape functions; $\boldsymbol{A}$ and $\boldsymbol{B}$ can be called the stiffness and mass matrices, in the context of the finite element method. However, (2.8) is an eigenvalue problem which was solved using the shift-invert Arnoldi technique, with the following boundary conditions:

$$\begin{aligned}
\hat{u}_x = \hat{u}_r = \hat{u}_\theta = 0 \qquad & on \quad \partial\Gamma_{body}, \\
\hat{u}_x = \hat{u}_r = \hat{u}_\theta = 0 \qquad & on \quad \partial\Gamma_{in}, \\
\hat{u}_r = \partial_r \hat{u}_x = \partial_r \hat{u}_\theta = 0 \qquad & on \quad \partial\Gamma_{top}, \\
-\hat{p}\boldsymbol{n} + Re^{-1}(\boldsymbol{\nabla}\hat{\boldsymbol{u}} + \boldsymbol{\nabla}\hat{\boldsymbol{u}}^T) \cdot \boldsymbol{n} = 0 \qquad & on \quad \partial\Gamma_{out}.
\end{aligned} \tag{2.9}$$

On the axis $\partial\Gamma_{axis}$ boundary conditions are specified based on the azimuthal mode number m: $\hat{u}_r = \partial_r \hat{u}_x = \partial_r p = 0$ for $m = 0$; $\partial_r \hat{u}_r = \partial_r \hat{u}_\theta = \hat{u}_x = \hat{p} = 0$ for $|m| = 1$; and $\hat{u}_r = \hat{u}_\theta = \hat{u}_x = \hat{p} = 0$ for $|m| \geqslant 2$.

2.3. *Numerical details for stability calculations*

The axisymmetric base flow fields and the generalised eigenvalue problem were solved numerically using the open-source software FreeFEM++ (http://www.freefem.org). The unknown velocity and pressure fields were spatially discretised using Taylor–Hood finite elements, specifically P_2 elements for velocity components and P_1 elements for pressure. Mesh generation and matrix assembly were carried out using FreeFEM++ (see Gopalakrishnan 2014 for implementation details). The base flow was computed following a procedure similar to that outlined in Marquet, Sipp & Jacquin (2008) and Gopalakrishnan, Pier & Biesheuvel (2014). Initially, a time-marching direct numerical simulation (DNS) of the Navier–Stokes equations (2.4*a*) and (2.4*b*), with the boundary conditions described earlier, was performed at a lower (stable) Reynolds number to obtain an initial flow field. This solution was then refined using a Newton–Raphson iterative method to compute the steady base flow by solving (2.5*a*) and (2.5*b*), both at the same and higher Reynolds numbers. The generalised eigenvalue problem (2.8) was solved using the implicitly restarted Arnoldi method with a shift-and-invert strategy, as described in Marquet *et al.* (2008). To identify the onset of the primary bifurcation, an initial guess of $\omega = 0$ was used, and the Reynolds number at which the growth rate σ changes sign (i.e. $\sigma > 0$) was determined. To identify the onset of the secondary bifurcation, an initial guess of $\omega = 0.5, 0.6, 0.7$ was used. The Reynolds number at which the growth rate σ changes its sign (i.e. $\sigma > 0$) was considered as the bifurcation Re.

https://doi.org/10.1017/jfm.2025.10871 Published online by Cambridge University Press

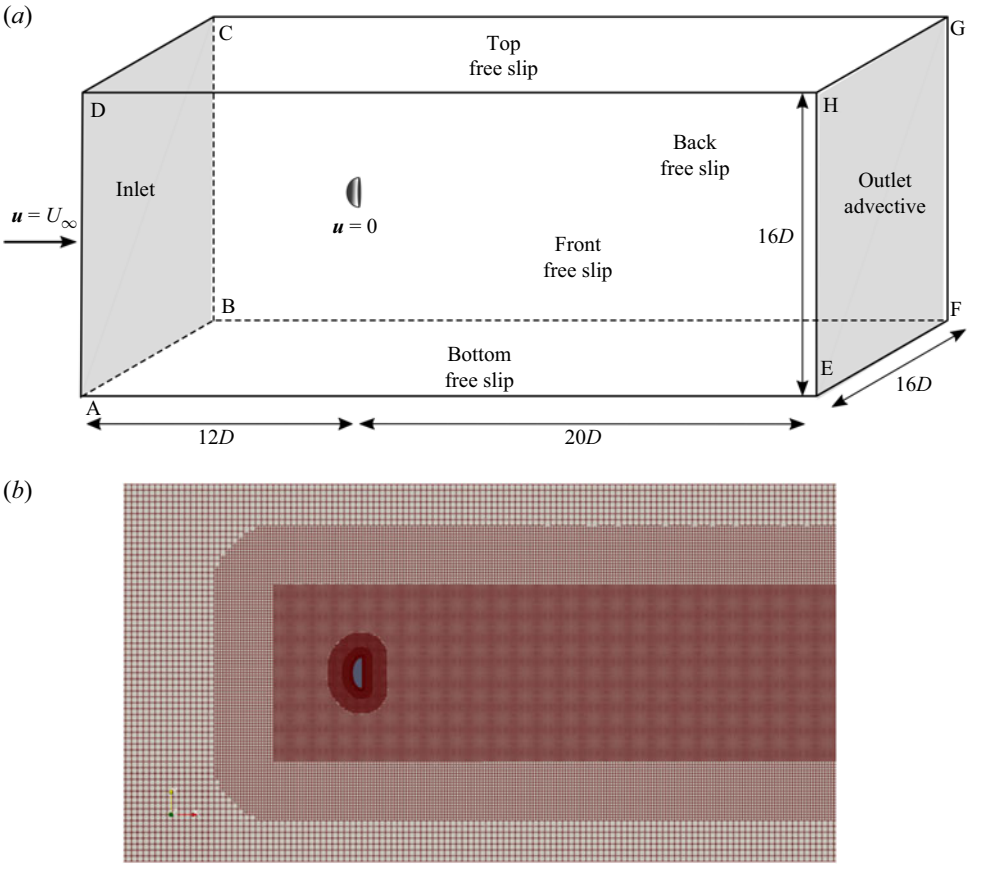


Figure 4. Flow over an elliptical cap: (*a*) schematic representation of the computational domain and boundary conditions at inlet (ABCD, $\boldsymbol{u} = (U_\infty, 0, 0)$), outlet (EFGH, $D\phi/Dt = 0$), top and bottom (CDHG and ABFE, $v = \mathrm{d}u/\mathrm{d}y = \mathrm{d}w/\mathrm{d}y = 0$), front and back (AEHD and BFGC, $w = \mathrm{d}u/\mathrm{d}z = \mathrm{d}v/\mathrm{d}z = 0$); (*b*) cross-sectional view ($x-y$ plane in $z = 0$) of hexahedral mesh generated using snappyHexMesh in OpenFOAM.

2.4. *Numerical details for three-dimensional DNS*

In addition to the global linear stability analysis, a three-dimensional numerical simulation was also performed using an open source computational fluid dynamics software, OpenFOAM (http://www.openfoam.com) version 2406, to study the laminar unsteady flow over an elliptical cap. Figure 4 presents the schematic of the computational domain, which incorporates an elliptical cap of $\chi = 0.6$. The origin of the coordinate system is located at the base of the elliptical cap model, similar to the one shown in figure 3(*a*).

Before deciding the computational domain, we carried out domain-independent simulations, as detailed in table 2, following previous studies (e.g. Saha 2004; Khan *et al.* 2020; Sarkar & De 2025). Based on these simulations, we arrived at a cuboid domain with a streamwise length of $32D$ and a cross-sectional area of $16D \times 16D$; here, D denotes the characteristic length of the elliptical cap. In this domain, the blockage is found to be only 0.30 %. A schematic of the computational domain is shown in figure 4.

We used the snappyHexMesh function of OpenFOAM to generate a mesh with hexahedral elements. Key mesh quality parameters include an aspect ratio of 7.3629, max non-orthogonality 53.1225 and average of 3.7581 and max skewness 0.6966. We use a

https://doi.org/10.1017/jfm.2025.10871 Published online by Cambridge University Press

large number of elements near the body and in the wake to resolve wake features of the flow accurately, as illustrated in figure 4(*b*). The mesh resolution (spatial resolution) in various regions of the domain was set as follows: near the body, $\Delta = 0.0025$, wake region, $\Delta = 0.05$ and far field, $\Delta = 0.2$.

To simulate the flow over the elliptical cap model, we use 'IcoFoam', which is a transient solver for an incompressible flow of the open source platform, OpenFOAM. This transient solver in OpenFOAM is designed for an incompressible flow that employs the pressure-implicit with splitting of operators (PISO) algorithm. The governing (2.4) were discretised using the second-order Crank–Nicolson scheme for time and the Gauss linear quadrature scheme for space. The PISO algorithm adopts a predictor–corrector strategy to iteratively solve for the velocity and pressure fields, ensuring proper coupling between these two fields. We use an inflow boundary condition as $u = U_\infty$ at the inlet, a no-slip boundary condition on the model surface and free-slip boundary conditions at the top, bottom and both sides of the domain. For the free-slip boundary conditions, the normal component of the velocity and the normal gradient of the tangential velocity component were made equal to zero. To maintain the numerical stability and the Courant–Friedrichs–Lewy (CFL) number less than 1, we used a time step size of $\Delta t = 0.0025$, resulting the mean CFL to be 0.01 and the maximum CFL to be 0.6. The convergence of the simulation was monitored based on the residuals, which were required to be below 10^{-6} for all variables.

2.5. *Validation: flow over sphere*

We have considered the flow past a sphere for validation of our numerical approach. The linear stability analysis for the flow over a sphere has been carried out to find the primary and secondary bifurcations, whereas the DNS for the sphere has been carried out at $Re = 300$ to investigate the mesh and domain independence. For the linear stability analysis, we have first simulated the flow past a sphere at Reynolds number, $Re = 50$, to get an initial guess flow field for the base flow calculation at the same Re. Following this calculation, we have calculated the base flow using the Newton–Raphson method, and the linear stability analysis has been carried out to investigate the growth of the small perturbations about this calculated base flow.

To assess the domain and the mesh independence for the stability analysis, the critical Reynolds number was examined for two different domain sizes (domain 1 and domain 2) and for three different meshes (mesh 1, mesh 2 and mesh 3). The computational domain was enclosed within a cylindrical boundary of radius $r_\infty = 30D$. For the initial simulation, the inlet and outlet boundaries were located at $x_{-\infty} = -30D$ and $x_\infty = 400D$, respectively, where D is the diameter of the sphere. In subsequent tests, the outlet was shifted to $x_\infty = 200D$. As shown in table 1, domain 2 with $x_\infty = 200D$ and mesh 2 was found to be sufficient to reproduce the critical Reynolds numbers accurately for the primary and secondary bifurcations, as these values compare well with the data reported in the literature (Meliga *et al.* 2009; Zheng, Pan & Ni 2023). Further, we calculated the coefficient of drag and the recirculation length from the base flow, which also compare well with the data of Pier (2008), as shown in figure 5.

Similarly, we have carried out the domain and mesh independence study for the three-dimensional (3-D) DNS for the flow over a sphere at $Re = 300$. The mean drag ($\overline{C}_D$) and lift ($\overline{C}_L$) coefficients and the Strouhal number (St) are calculated for different domains and meshes. One can notice that the data for case 2 compares well with the data reported in the literature (Johnson & Patel 1999; Constantinescu & Squires 2000; Kim & Choi 2002), as seen in table 2.

https://doi.org/10.1017/jfm.2025.10871 Published online by Cambridge University Press

Case	Domain	Mesh	Domain Ω $x_{-\infty} \times r_{\infty} \times x_{\infty}$	Δx_{min}	Δx_{max}	No. of triangles N_t	Re_{c1}	Re_{c2}
Case 1	Domain 1	Mesh 1	$-30D \times 30D \times 400D$	0.0114	2.465	74497	212.2	281.5
Case 2	Domain 2	Mesh 1	$-30D \times 30D \times 200D$	0.0130	1.526	54659	212.1	281.5
Case 3	Domain 2	Mesh 2	$-30D \times 30D \times 200D$	0.0072	2.413	69637	212.7	280.9
Case 4	Domain 2	Mesh 3	$-30D \times 30D \times 200D$	0.0049	2.559	76588	212.7	280.9
						Meliga *et al.* (2009)	212.6	280.7
						Zheng *et al.* (2023)	212.68	280.8

Table 1. Validation of flow over sphere by comparing Re for primary and secondary bifurcations with grid and domain independence by global linear stability analysis. The same mesh distribution is used for cases 1 and 2, with a varying streamwise domain length to check the influence of domain extent on the stability results.

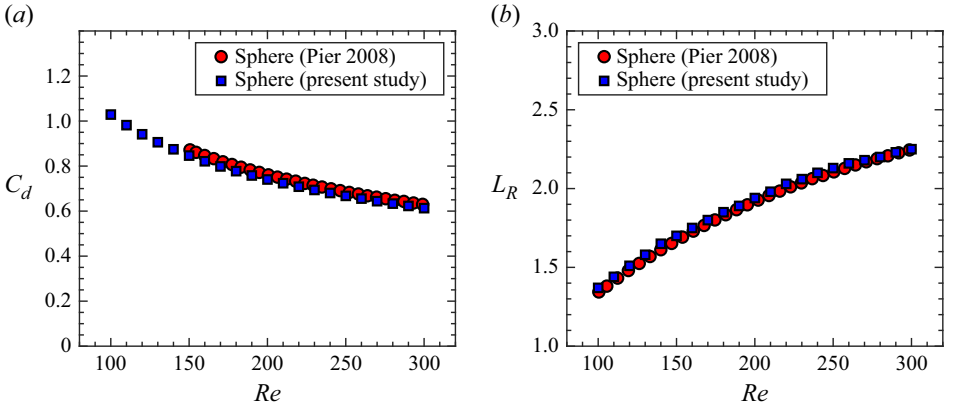


Figure 5. Comparison with Pier (2008). (*a*) Coefficient of drag C_d and (*b*) recirculation length L_R of the base flows for various aspect ratios.

Case	Domain $L_x \times L_y \times L_z$	Mesh	Δx_f	Δx_w	Δx_b	Cells	$\overline{C}_D$	$\overline{C}_L$	St
Case 1	Domain 1 ($32D \times 16D \times 16D$)	Mesh 1	0.4	0.1	0.01525	1,537,230	0.666	0.073	0.134
Case 2	Domain 1 ($32D \times 16D \times 16D$)	Mesh 2	0.2	0.05	0.00625	12,386,768	0.664	0.064	0.134
Case 3	Domain 1 ($32D \times 16D \times 16D$)	Mesh 3	0.1	0.05	0.003125	25,635,406	0.662	0.069	0.134
Case 4	Domain 2 ($45D \times 20D \times 20D$)	Mesh 2	0.2	0.05	0.00625	16,975,568	0.663	0.069	0.134
Case 5	Domain 3 ($60D \times 30D \times 30D$)	Mesh 2	0.2	0.05	0.00625	24,838,368	0.662	0.0689	0.134
	Johnson & Patel (1999)						0.656	0.069	0.137
	Constantinescu & Squires (2000)						0.655	0.065	0.136
	Kim & Choi (2002)						0.657	0.067	0.134

Table 2. Mesh and domain independence test cases for the flow over a sphere at $Re = 300$. We have finally chosen case 2 for the DNS reported in this article. Here, Δx_f, Δx_w and Δx_b denote the mesh spacing at the far field, wake and body, respectively.

2.6. *Experimental methods and techniques*

All the experiments reported here were performed in a water tunnel. It has a test section of 180 in width, 250 in depth and 460 mm in length. The flow speed in the tunnel is controlled by a speed controller, and it can be varied from 10 to 100 mm s^{-1}. This tunnel was used in various previous works (e.g. Bhattacharyya *et al.* 2022; Sunil, Kumar & Poddar

https://doi.org/10.1017/jfm.2025.10871 Published online by Cambridge University Press

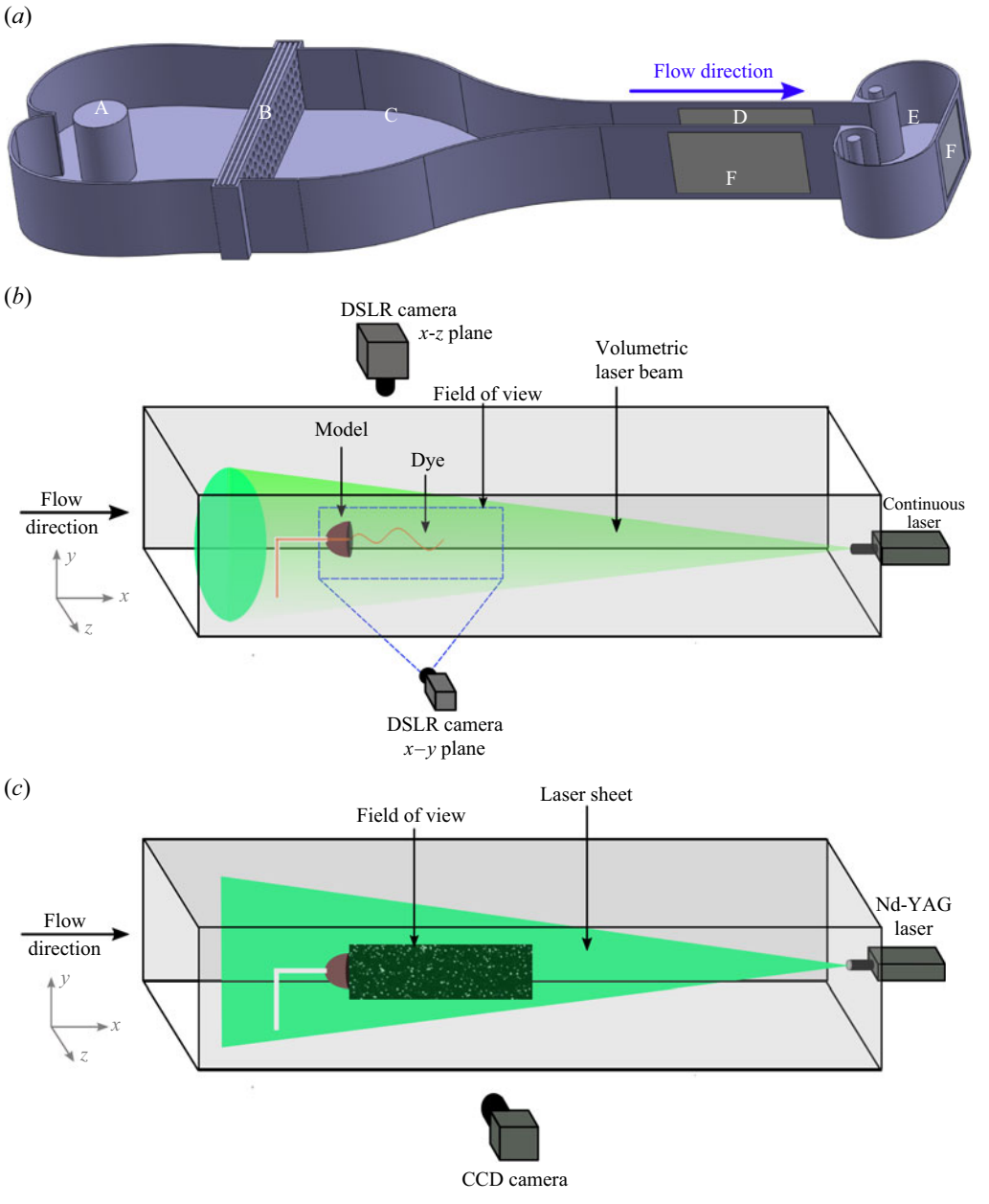


Figure 6. Schematic of the experimental set-up with right-handed Cartesian coordinate system (x, y, z), where x, y and z denote the streamwise, wall-normal and spanwise directions, respectively. (*a*) Water tunnel A: plenum, B: honeycomb and screen, C: contraction, D: test section, E: reticulation chamber (send water back to plenum) and F: transparent window. (*b*) Experimental set-up for simultaneous LIF visualisations. where the flow is from left to right, as shown by an arrow. (*c*) Schematic sketch for 2D-PIV in the $x-y$ plane. (a similar set-up was used for the other plane, as well).

2022; Khan *et al.* 2023). Figure 6 shows a simple schematic of the present experimental arrangement in the test section of the water tunnel. The model placed in the middle of the test section using a support-sting (see figure 6) has a base diameter of 10 mm. The support-sting was made of a hollow tube of diameter 1.1 mm to inject dye into the flow.

https://doi.org/10.1017/jfm.2025.10871 Published online by Cambridge University Press

We may mention that Gumowski *et al.* (2008) and Szaltys *et al.* (2012) also used a similar dye injection system.

In the present study, the laser-induced fluorescence (LIF) technique was used for flow visualisation (Sunil *et al.* 2022). We have used Rhodamine-B as the dye for flow visualisations. Since the dye injection tube (made of stainless steel) has a small diameter ($\approx$1.1 mm), it does not significantly affect the uniform flow in the test section. A continuous laser (5 W) is used to illuminate the dye. The flow rate of the dye solution is carefully controlled such that a minimum amount of dye is released in the flow to avoid its influence on the wake structure. The flow visualisation images were acquired using a DSLR camera (Nikon, model D850, 3820 pixels $\times$2460 pixels) at 30 frames per second for a region of interest of 200 mm $\times$ 100 mm. More than 9000 images were acquired for each experimental run, which were then analysed using the MATLAB image processing tool. Flow characteristics, such as the vortex shedding frequency, were calculated using the time series of these acquired images. We also carried out simultaneous dual-plane flow visualisations using two cameras in two different orthogonal planes for better characterisations of the wake.

The velocity fields in two different planes were obtained using the 2-D particle-image-velocimetry (2D-PIV) technique. The PIV measurements were performed in the wake region, downstream of the model, as shown in figure 6(*c*). The set-up for the same LIF technique was modified for the PIV measurements by replacing the continuous laser and the DSLR camera with a Nd:YAG double-pulsed laser (Quantel, EverGreen model with 200 mJ/pulse) and compatible CCD cameras (TSI, USA) with resolutions of 3312 $\times$ 2488 pixels (8 MP) at 1.45 Hz and 4912 $\times$ 3280 pixels (16 MP) at 1 Hz in double exposure mode, respectively. The experimental measurements were made using the first CCD camera (8 MP) unless otherwise stated explicitly. The flow was seeded with hollow glass spheres of approximate diameter 10 μm. The required flow region was illuminated with $\approx$1 mm thickness of laser sheet, and 1200 snapshots (600 pairs) were acquired for each case for an acquisition time of $\approx$414 s. The acquired images were post-processed using ProVisionXS (IDTpiv), with a 32$\times$32 pixels correlation window. The uncertainty in velocity was estimated to be approximately 3 % of the maximum streamwise velocity. This PIV system and the processing software were also used in our various previous studies (Balamurugan & Mandal 2017; Sunil *et al.* 2022; Aniffa *et al.* 2023).

2.7. *Proper orthogonal decomposition analysis*

Proper orthogonal decomposition (POD) helps identify coherent structures in unsteady flows and provides additional insights into the underlying flow dynamics. We briefly describe the technique, which is based on decomposing the fluctuating velocity field into spatial modes and their corresponding temporal coefficients.

Briefly, this technique provides basis functions $\boldsymbol{\Phi}^{(k)}(\boldsymbol{x})$ that can represent a random function, such as a fluctuating velocity field $\boldsymbol{v}'(\boldsymbol{x}, t)$, as (Berkooz, Holmes & Lumley 1993)

$$\boldsymbol{v}'(\boldsymbol{x}, t) \approx \sum_{i=1}^{k} a^{(k)}(t)\, \boldsymbol{\Phi}^{(k)}(\boldsymbol{x}), \tag{2.10}$$

where, a, $\boldsymbol{\Phi}$ and k represent the time coefficient, the spatial POD mode shape and the mode index, respectively. It should be noted that the fluctuating velocity field, $\boldsymbol{v}'(\boldsymbol{x}, t)$, comprises the fluctuating streamwise velocity, u'_x (= instantaneous velocity, u_x – mean velocity $\overline{u}_x$) and the fluctuating transverse velocity, u'_y (= instantaneous velocity, u_y, – mean velocity, $\overline{u}_y$), in the present study. Here, the POD mode shapes are obtained using the method of snapshots (Sirovich 1987). The fluctuating flow field $\boldsymbol{v}'$ from each PIV snapshot

https://doi.org/10.1017/jfm.2025.10871 Published online by Cambridge University Press

is arranged into a matrix A, and the covariance matrix C is then obtained as $C = A^T A$. The eigenvalues λ_k of the matrix C are then computed, which indicate the energy levels associated with each POD mode. The spatial POD modes are calculated as

$$\boldsymbol{\Phi}_k = \sum_{i=1}^{M} \phi_i^k \boldsymbol{v}_i', \tag{2.11}$$

where M is the number of snapshots and ϕ_i^k is the i^{th} component of the k^{th} eigenvector of the matrix C. The time coefficients (a_k) are then obtained using the inner product of $\boldsymbol{v}'$ and $\boldsymbol{\Phi}_k$ as $a_k = (\boldsymbol{v}', \boldsymbol{\Phi}_k)$. The relative energy, E_r (in %), of the POD modes is calculated as

$$E_r = \frac{\lambda_r}{\sum_{i=1}^{n} \lambda_r} \times 100\,\%. \tag{2.12}$$

The reader may refer to Mandal, Venkatakrishnan & Dey (2010) and Dutta *et al.* (2022), for further details.

3. Base flow fields and global stability characteristics

The present section considers the base flow fields obtained for moderate Reynolds numbers at varying aspect ratios. We consider the elliptical cap bluff body to characterise the global flow behaviour at varying aspect ratios. The effect of the geometrical shape used to model the bluff body (elliptical/spherical) is discussed subsequently. The numerically obtained results are compared with the experimental observations in the next section.

3.1. *Basic velocity fields*

The steady axisymmetric base flow field for an elliptical cap at $Re = 100$ is illustrated in figure 7, where the streamlines are superimposed on contour of the azimuthal vorticity $\omega_\theta \equiv \partial_x u_r - \partial_r u_x$ for varying aspect ratios. The flow separates at the downstream edge of the axisymmetric bluff body and rejoins in the wake to form a toroidal recirculating region. The shear layer developing on the surface of the elliptical cap rolls up at its base, which is the region where the vorticity fields have their maxima. This is evident at lower aspect ratios wherein the spatial gradients of vorticity are more pronounced in the lee side of the bluff body, as shown in figure 7. It can also be noted that the length of the recirculation bubble decreases with increasing aspect ratio, which is expected as the spatial extent of the favourable pressure gradient increases with χ. Similar observations have been made for flow past planar symmetric bluff bodies with increasing aspect ratio (Chiarini *et al.* 2022).

The recirculation length is considered as the streamwise distance from the base of the model to the stagnation point in the wake along the centreline, and it is normalised by the base diameter D. The dimensionless recirculation length L_R for various Reynolds numbers is presented in figure 8(*a*). It can be seen that L_R decreases with increasing aspect ratio for a fixed value of the Reynolds number. The spatial extent of the recirculation zone is of relevance as the nonlinear interactions between the modes take place within this absolutely unstable region, thereby effectively acting as a wave maker (Meliga *et al.* 2009). The observed trend of L_R with Re and χ can be summarised by re-scaling it using the Reynolds number as a parameter, which is shown in figure 8(*b*). We can see that the re-scaled value of L_R is approximately a constant (∼0.3–0.4) for different values of χ, as compared with the unscaled variation (figure 8*b*). The maximum reverse-flow velocity within the recirculating region U_{rev} (normalised by the free-stream velocity U_∞) is another quantity of interest to quantify the base flow characteristics. Its variation with aspect ratio

https://doi.org/10.1017/jfm.2025.10871 Published online by Cambridge University Press

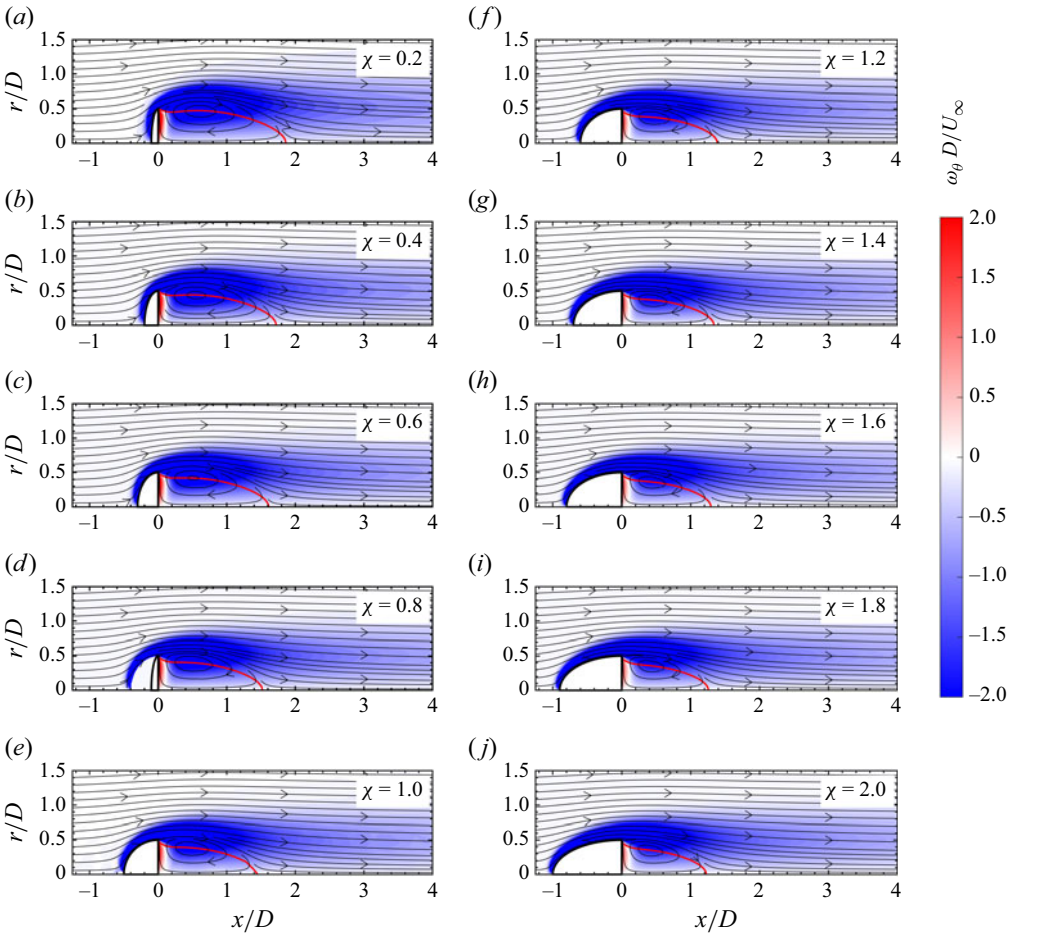


Figure 7. Base flow of elliptical shapes for different aspect ratios $\chi = 0.2$ to 2.0 at $Re = 100$. Streamlines are plotted on top of a vorticity map ($\omega_\theta = \partial_x u_r - \partial_r u_x$), with the symmetric blue-to-red colour map in the range of $-2 \leqslant \omega_\theta \leqslant 2$. The red solid line represents the recirculation zone.

for increasing values of Re is shown in figure 8(c). As observed for L_R, the maximum reverse-flow velocity also decreases with increasing aspect ratio for a fixed value of the Reynolds number. The re-scaled values of U_{rev}, as shown in figure 8(d), collapse to a single curve for different Reynolds numbers and vary approximately from 0.03 to 0.05 for different values of χ. However, as the unscaled L_R and U_{rev} decrease with increasing χ, we expect increasing aspect ratio to have a stabilising effect on the flow.

3.2. *Global stability analysis*

The global linear stability analyses were carried out on the base flow fields described in the preceding subsection. Figure 9 shows the eigenvalue spectrum corresponding to the flow past a hemisphere with $\chi = 1$ for different values of the azimuthal mode number m. As observed in earlier studies on bluff-body flows, the leading global mode corresponds to $m = 1$ with the primary bifurcation (shown in figure 9a) being a stationary one with $\omega = 0$ at the critical Reynolds number $Re_{c1} = 170.1$. At a higher Reynolds number, the flow undergoes a Hopf bifurcation with a non-zero value for ω at $Re_{c2} = 189.9$ (shown in figure 9b). The Strouhal number corresponding to the secondary bifurcation is found to be

https://doi.org/10.1017/jfm.2025.10871 Published online by Cambridge University Press

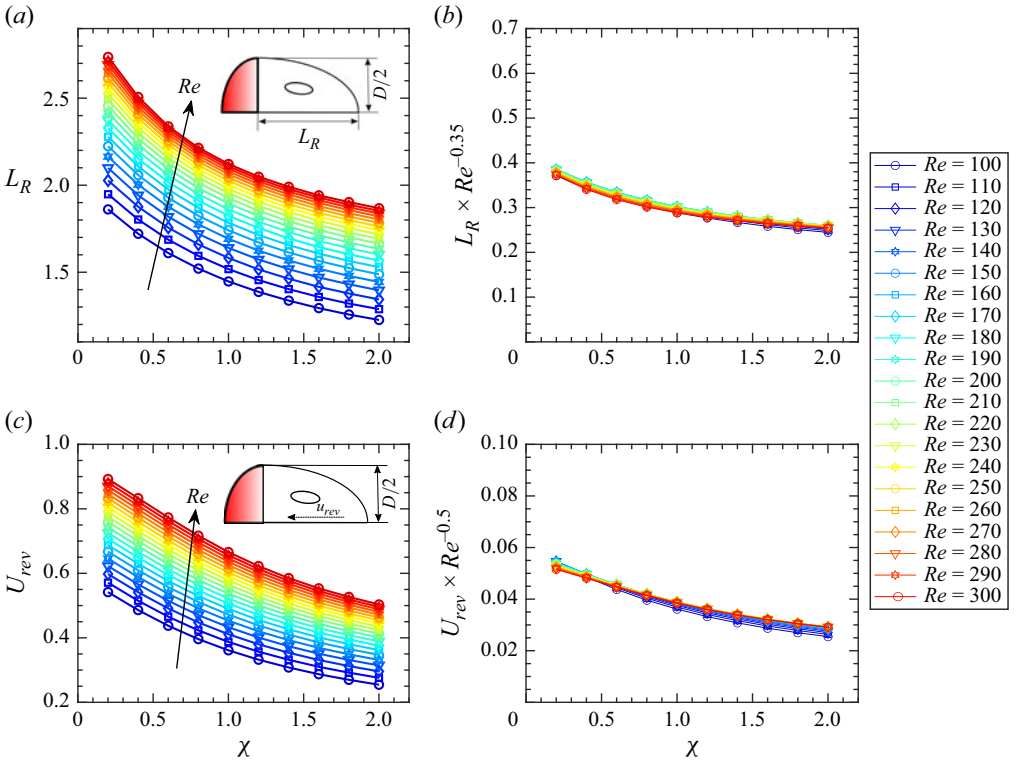


Figure 8. (*a*, *c*) Recirculation length L_R and the maximum reverse-flow velocity U_{rev} within the recirculation zone as a function of the aspect ratio for increasing values of Reynolds numbers (denoted using an arrow). (*b*, *d*) Re-scaled values of L_R and U_{rev}. Parameter settings: $100 \leqslant Re \leqslant 300$.

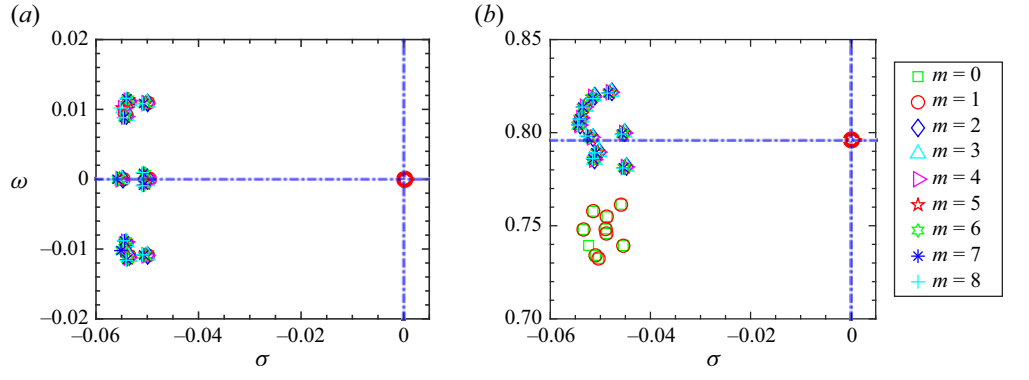


Figure 9. Eigenvalue spectrum for different azimuthal mode numbers m corresponding to the (*a*) primary bifurcation at $Re_{c1} = 170.1$, and the (*b*) secondary bifurcation at $Re_{c2} = 189.9$. Parameter settings: $\chi = 1$; hemisphere.

0.1267. These values are in excellent agreement with those reported in Jiménez-González *et al.* (2019) for the case of a hemisphere.

Figure 10 shows the variation of the temporal growth rate σ corresponding to the leading global mode as a function of the Reynolds number at different aspect ratios. It can be seen that the critical Reynolds number increases with increasing aspect ratio for

https://doi.org/10.1017/jfm.2025.10871 Published online by Cambridge University Press

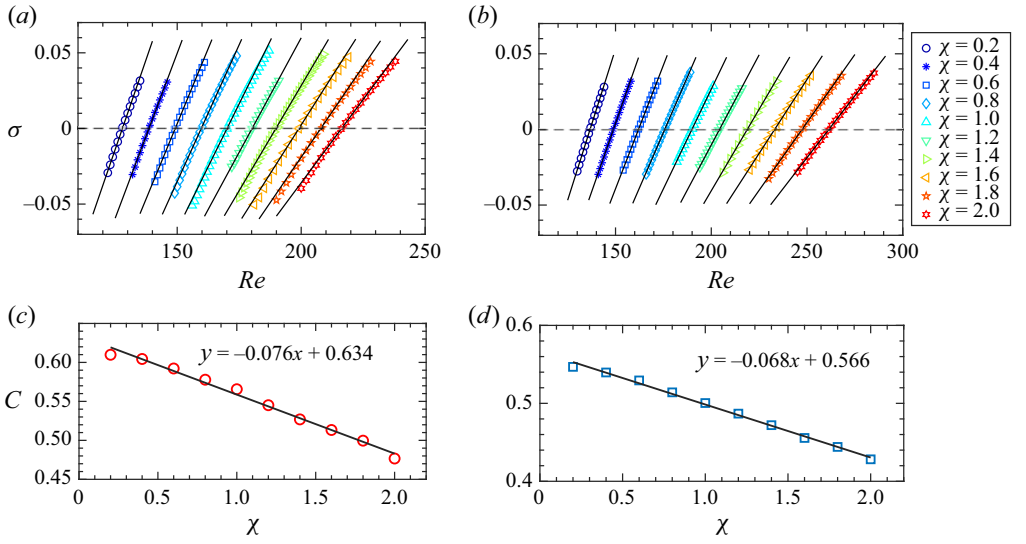


Figure 10. Growth rate as a function of the Reynolds number for various aspect ratios of elliptical shape. (*a*) Primary (stationary) bifurcation and (*b*) secondary (oscillatory) bifurcation, with a modified constant value for the linear fit. (*c–d*) Values of the constant C (defined in (3.1)) for different aspect ratios for primary bifurcation and for secondary bifurcation.

both the primary and secondary bifurcations, which are shown in figures 10(*a*) and 10(*b*), respectively. One can notice that σ varies almost linearly with Re. It can be related using the Landau model (Landau 1944) as

$$\sigma = C(Re - Re_c)\frac{\nu}{D^2}, \tag{3.1}$$

where C is a constant, which can vary based on the shape of the bluff body and the nature of bifurcation, and D is a typical length scale associated with the geometry. Earlier studies have reported $C = 0.2$ for flow past a cylinder, whereas $C = 0.6$ for the wake of a sphere (Provansal, Mathis & Boyer 1987; Sreenivasan, Strykowski & Olinger 1987; Ormières & Provansal 1999; Thompson, Leweke & Provansal 2001; Schouveiler & Provansal 2002; Provansal, Schouveiler & Leweke 2004). Furthermore, different values have been chosen in the literature for the flow past a sphere corresponding to the primary and secondary bifurcations. For instance, Ghidersa & Dušek (2000) and Thompson *et al.* (2001) considered $C = 0.5$ for the secondary bifurcation, whereas Provansal *et al.* (2004) considered $C = 0.6$ for both primary and secondary bifurcations. In the present study, we have used a linear fit to determine the value of constant C as a function of the aspect ratio χ, which is shown in figure 10 in panels (*c*) and (*d*) for the primary and secondary bifurcations, respectively. We can see that the value of C decreases with χ and falls in the range of 0.4–0.6.

The spatial distribution of the eigenmodes at Re_{c1} and Re_{c2} for $\chi = 1$ are shown in figures 11 and 12, respectively. The structure of $\hat{u}_x$, $\hat{u}_r$ and $\hat{u}_\theta$ corresponding to the primary bifurcation shows that the leading global mode is dominated by axially extending streamwise disturbances. As the leading global mode corresponds to the azimuthal mode number $m = 1$, the axial velocity perturbation is opposite on the other side of the axis of revolution. The radial and azimuthal velocity perturbations are primarily dominant in the near-wake region. These spatial distributions are typical of stationary bifurcations observed in axisymmetric flows past bluff bodies, which we have also observed using

https://doi.org/10.1017/jfm.2025.10871 Published online by Cambridge University Press

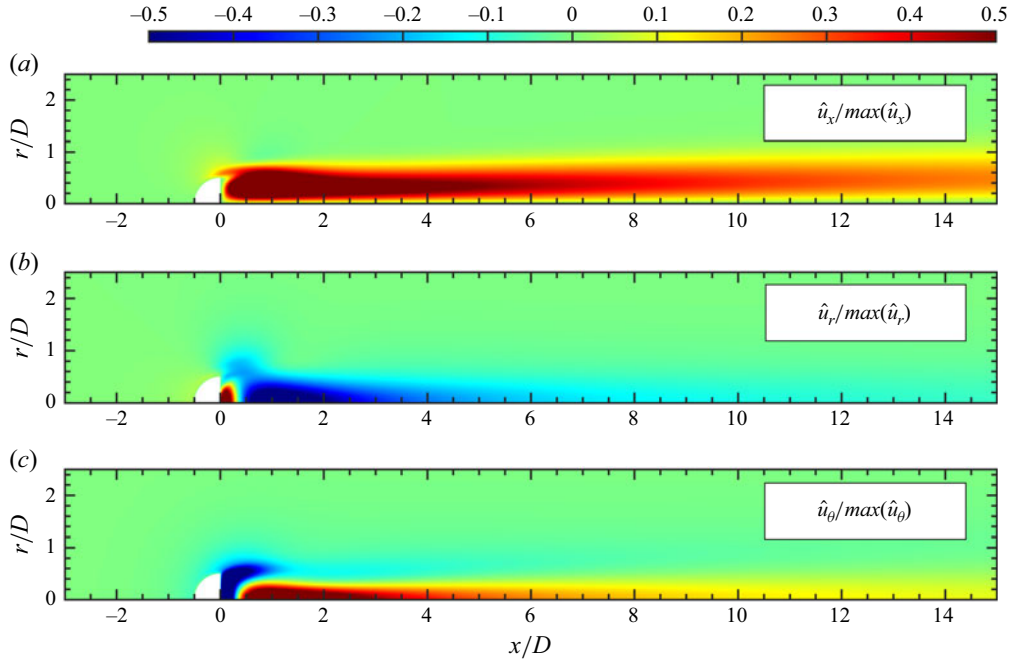


Figure 11. Spatial distribution of the leading global mode at the primary stationary bifurcation. The real part of the velocity perturbations normalised by their maxima: (*a*) $\hat{u}_x$, (*b*) $\hat{u}_r$ and (*c*) $\hat{u}_\theta$. Parameter settings : $Re = 170.1$, $\chi = 1$, $m = 1$.

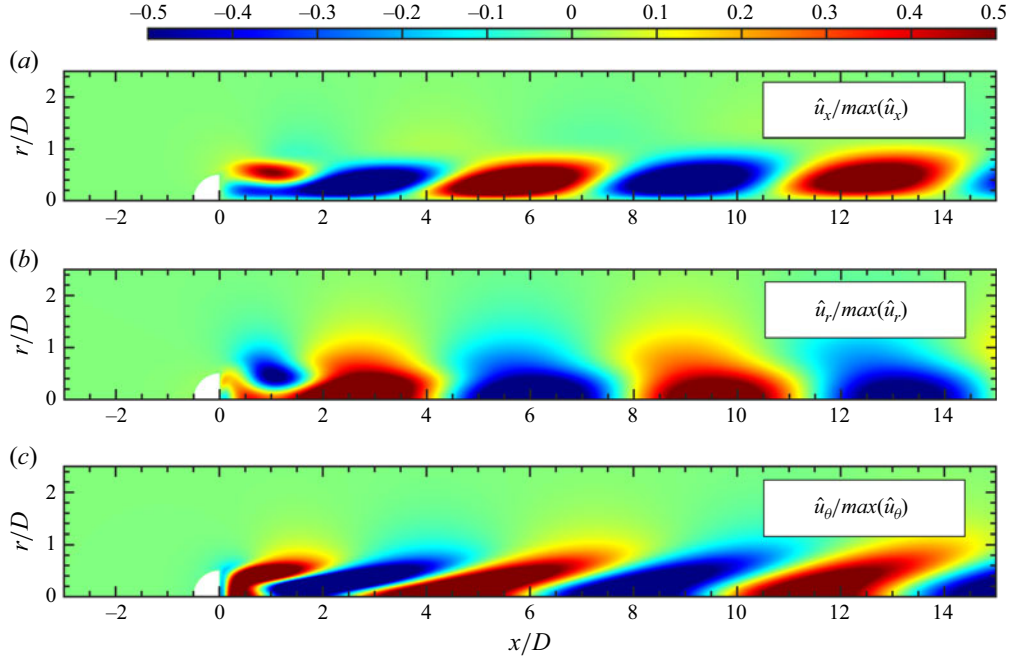


Figure 12. Spatial distribution of the leading global mode at the secondary oscillatory bifurcation. The real part of the velocity perturbations normalised by their maxima: (*a*) $\hat{u}_x$, (*b*) $\hat{u}_r$ and (*c*) $\hat{u}_\theta$. Parameter settings : $Re = 189.9$, $\chi = 1$, $m = 1$.

https://doi.org/10.1017/jfm.2025.10871 Published online by Cambridge University Press

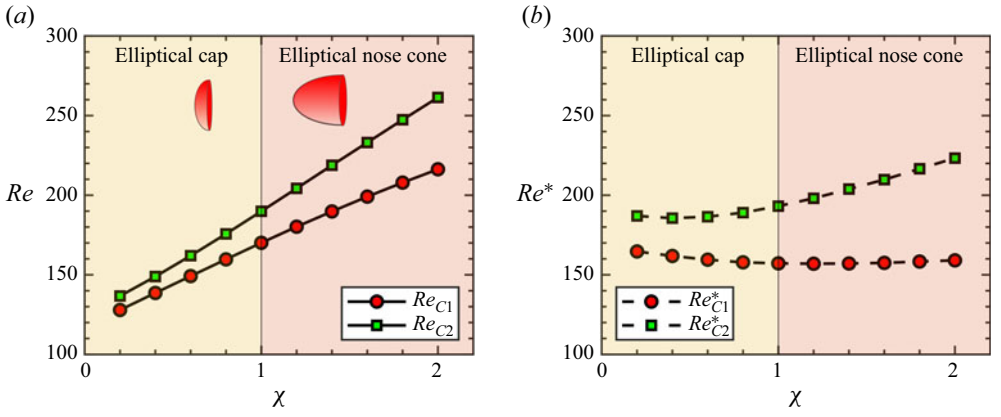


Figure 13. (*a*) Critical Reynolds numbers corresponding to the primary (Re_{c1}) and secondary (Re_{c2}) bifurcations as a function of the aspect ratio χ. (*b*) Critical Reynolds numbers rescaled using the recirculation length L_R and the maximum reverse-flow velocity U_{rev} such that $Re^* = U_{rev} L_R/\nu$ as a function of the aspect ratio. It can be seen that the rescaled critical Reynolds number corresponding to the primary bifurcation remains approximately a constant at different values of χ.

dual-plane experimental flow visualisations (discussed in the subsequent section). On the other hand, the leading global mode at Re_{c2} has spatially periodic variations along the axial direction, which is characteristic of an oscillatory bifurcation, as shown in figure 12. Similar spatial distributions are also observed for other aspect ratios.

Figure 13(*a*) shows the variation of the critical Reynolds number corresponding to the primary (Re_{c1}) and secondary (Re_{c2}) bifurcations as a function of the aspect ratio. The aspect ratio χ has been varied from 0.2 to 2.0 in the present study. The values of Re_{c1} and Re_{c2} at $\chi = 2$ are 216.3 and 261.4, respectively, which are in excellent agreement with Bohorquez *et al.* (2011) ($L/D = 1$ in their study). Similarly, the values of Re_{c1} and Re_{c2} at $\chi = 0.2$ are found to be 127.9 and 136.7, which are comparable to the corresponding values of 116.9 and 125.3 as reported by Meliga *et al.* (2009) for a disk. It should be noted that the shape of the present model at $\chi = 0.2$ is similar to a disk, but not a complete disk. Further, we find the primary bifurcation at $Re = 170.1$ for the model with $\chi = 1.0$ (a hemisphere), which is in good agreement with the findings of Jiménez-González *et al.* (2019), who also used a steady axisymmetric base flow for linear stability analysis. Kim & Choi (2003) reported the onset of primary bifurcation in the range of $180 < Re < 190$ and the secondary bifurcation in the range of $200 < Re < 210$ for hemispherical geometries. These observations are found to be consistent with the present trends.

We can see that increasing the aspect ratio has a stabilising effect as mentioned earlier. This is consistent with the fact that L_R, which characterises the spatial extent of the absolutely unstable region, and U_{rev}, which is a measure of the growth of disturbances which travel upstream, both decrease with increasing χ. Furthermore, the boundary layer thickness at the point of separation increases with an increase in the length of the bluff body, leading to a thickening of the shear layer resulting in an increased diffusion of the shear layer and a weaker instability. Using L_R and U_{rev} as the length and velocity scales, we have rescaled the critical Reynolds number, which is shown in figure 13(*b*) as a function of the aspect ratio. Interestingly, the rescaled critical value of the Reynolds number corresponding to the primary bifurcation is approximately a constant for different values of χ. The critical Reynolds number corresponding to the secondary bifurcation shows a larger variation within the investigated range of aspect ratios. This may be due to the consideration of axisymmetric base flow even after primary bifurcation, which

https://doi.org/10.1017/jfm.2025.10871 Published online by Cambridge University Press

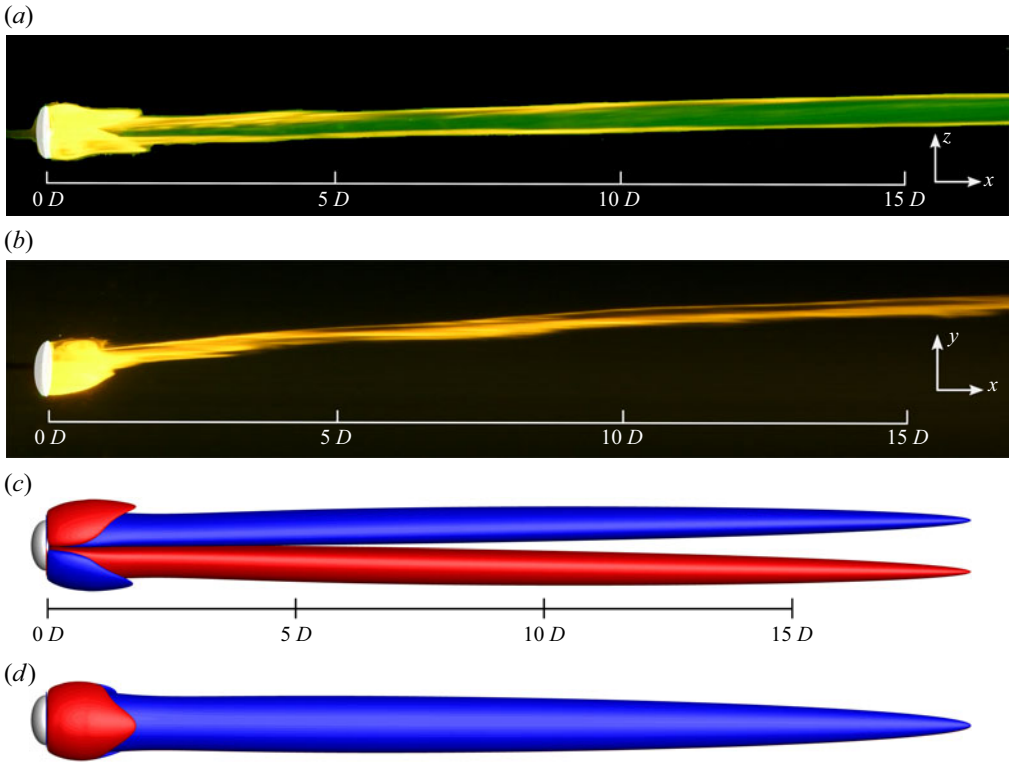


Figure 14. (*a–b*) The LIF visualisations of flow (from left to right) past an elliptical cap of aspect ratio $\chi = 0.6$ at $Re \approx 150$. The Reynolds number is slightly above the critical value corresponding to the primary bifurcation. The stationary double-threaded bifid structure of the wake is clearly visible with a planar symmetry. (*a*) Top view in the x–z plane, and (*b*) side view in the x–y plane. (*c–d*) Iso-surfaces of vorticity, $\omega_x = \partial w/\partial y - \partial v/\partial z$ obtained from DNS data for the elliptical cap at $\chi = 0.6$ and $Re = 153$. (*c*) Top view in the x–z plane, and (*d*) side view in the x–y plane.

is actually not axisymmetric beyond the primary bifurcation (e.g. Pier 2008). However, this aspect needs to be investigated further. Considering the scaled Re_* as shown in figure 13(*b*), one can rewrite the (3.1) as

$$\sigma = C^*(Re^* - Re_c^*)\frac{\nu}{L_R^2}, \tag{3.2}$$

where C^* is a constant, and $Re^* = U_{rev}L_R/\nu$. The Landau constant, C^*, is found to be approximately 1 for both the primary and secondary bifurcations.

To summarise, we have presented the base flow fields and the stability characteristics corresponding to the bubble-shaped geometries modelled as an elliptical cap in this section. We now proceed to compare the obtained results with experimental measurements and visualisations in the following section.

4. Comparison with DNS and experimental observations

For experimental characterisations, we have carried out simultaneous dye flow visualisations in two different orthogonal planes. For quantitative flow visualisations, we have also carried out the PIV measurements. Figures 14(*a*) and 14(*b*) show the simultaneous flow visualisations in the x–z and x–y planes, respectively. These

https://doi.org/10.1017/jfm.2025.10871 Published online by Cambridge University Press

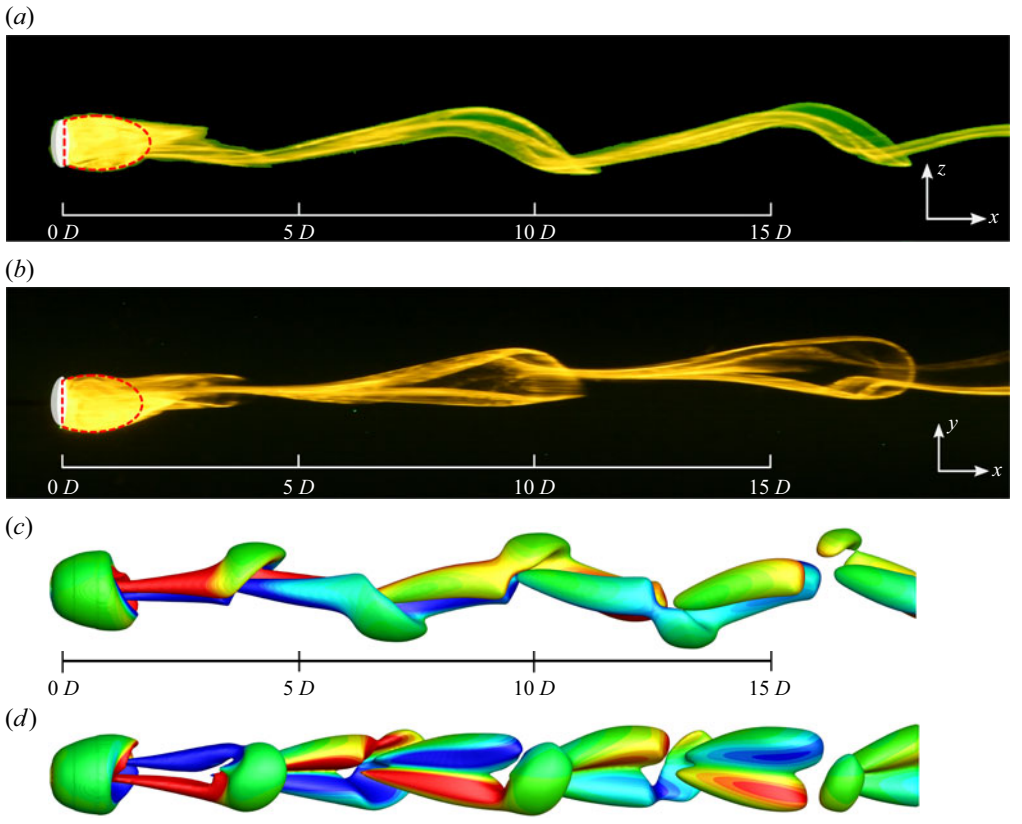


Figure 15. (*a–b*) The LIF visualisation corresponding to the secondary oscillatory bifurcation for $\chi = 0.6$ at $Re \approx 162$. The trailing counter-rotating vortices get connected to each other resulting in the formation of skewed loops.(*a*) Top view in the $x-z$ plane. (*b*) Side view in the $x-y$ plane. The dash line shows the recirculation region and $L_R \approx 1.8$ whereas the base flow, $L_R = 1.98$. (*c–d*) Iso-surfaces of λ_2 criterion obtained from the DNS data for the elliptical cap model with $\chi = 0.6$ at $Re = 167$. (*c*) Top view $x-z$ plane. (*d*) Side view $x-y$ plane.

visualisations are obtained using the LIF technique at $Re = 150$, which is slightly above the critical value $Re_{c1} = 149.2$ corresponding to the primary bifurcation. The bubble shape is modelled as an elliptical cap of aspect ratio $\chi = 0.6$. The wake is characterised by two trailing counter-rotating vortices with the injected dye being trapped in the vortex cores. This observation is further supported by the DNS data, as shown in figures 14(*c*) and 14(*d*) in terms of the iso-surface of streamwise vorticity, $\omega_x = (\partial w/\partial y - \partial v/\partial z)$. However, this results in a two-threaded structure which is clearly visible in the top view (x–z plane) shown in figure 14(*a*). The observed mode manifests itself through a tilting of the recirculating region in the near wake of the bluff body, and is attributed to the breaking of axisymmetry rather than to the splitting of a thread into two. The counter-rotating vortices in the wake induce a velocity along the centreline resulting in a convective displacement of the two threads with respect to each other. This results in an increase in the gap between the threads along the axial direction which can also be seen in the top view. The stationary nature of the bifurcation is also clearly captured, as no oscillation is observed for the dye streaks. Furthermore, the flow visualisations clearly indicate that the axisymmetry is replaced by a planar symmetry.

As the Reynolds number is increased further, the flow undergoes an oscillatory bifurcation at $Re_{c2} = 162$ for $\chi = 0.6$. This is shown in figures 15(*a*) and 15(*b*) wherein

https://doi.org/10.1017/jfm.2025.10871 Published online by Cambridge University Press

the trailing counter-rotating vortices get connected to each other, resulting in the formation of strongly skewed loops which get convected downstream. We may note that these visualisations in two different planes were also performed simultaneously using two cameras. However, the flow retains the plane of symmetry selected at the previous bifurcation, as seen in the flow visualisations in the cross-flow plane. One may notice in figure 15(*b*) that there exists a lateral displacement of the shed vortices while moving downstream. This is due to the fact that the velocity of the counter-rotating vortices in the wake is always directed in one way (see Gumowski *et al.* 2008), resulting a lateral movement. The DNS data, as shown in figures 15(*c*) and 15(*d*), in terms of the iso-surfaces of λ_2 (Jeong & Hussain 1995), also show similar results visualised using the LIF technique.

Figure 16(*a*) schematically shows the cross-flow plane for the LIF visualisation. We have carried out cross-flow visualisations for two different models with aspect ratios, $\chi = 0.6$ and $\chi = 2.0$. Figures 16(*b*) and 16(*c*) show the LIF visualisations at different instants of time within a period of oscillation, for aspect ratios $\chi = 0.6$ at $Re \approx 162$ and $\chi = 2.0$ at $Re \approx 249$, respectively. It should be noted that a laser sheet from the continuous laser was used in the cross-flow plane for this visualisation (figure 16*a*). However, one can clearly notice that there exists a plane of symmetry in these visualisations. Although the same holding device was used to hold both the models, the plane of symmetry changes due to the change of the aspect ratio, as seen in figures 16(*b*) and 16(*c*). It was also found that the plane of symmetry for a particular model does not change its orientation with an increase in Reynolds number beyond the secondary bifurcation. However, it must be noted that, although the angular orientation of this plane in principle is selected by the vertical orientation of the support system in experiments, the perturbations induced by the holding device may indeed modify it, resulting in the selection of a different symmetry plane. These observations are in excellent agreement with those made for flows past other axisymmetric bluff bodies where the vortex shedding regimes are characterised by the rotation of a symmetry plane (Fabre *et al.* 2008) leading to a 'kinking' of vortex threads (Shenoy & Kleinstreuer 2008), resulting in a shifted hairpin shedding (Meliga *et al.* 2009; Bobinski *et al.* 2014).

Similar flow features were observed at other aspect ratios. The flow fields at different time instants obtained using the LIF technique for $\chi = 2$ at the Reynolds number corresponding to the secondary bifurcation are shown in figure 17. The observed wake structure reveals that the flow fields indeed do exhibit a planar symmetry. Furthermore, it can be noticed that the extent of the recirculating region is considerably smaller in comparison with the flow fields observed at $\chi = 0.6$ (shown in figure 15*b*). The critical Reynolds numbers, Re_{c1} and Re_{c2}, corresponding to the primary and secondary bifurcations observed experimentally, agree well with the predictions made using the global linear stability analyses of the axisymmetric base flow fields within the range of aspect ratios considered in the present study.

To further quantify and compare the experimental observations with the linear stability analyses, we have measured the vortex shedding frequency and the wavelength of the wake structure, as shown in figure 18. The time-series data of the intensity of the images are obtained at different spatial locations, as shown in figure 18(*a*). These locations are carefully chosen such that they are slightly offset from the axis, which ensures that a continuous stream of images with finite intensities is obtained. The data are collected over an interval of 2 min, which corresponds to approximately 3600 images. The shedding frequency is then obtained by performing a Fourier transform, as shown in figure 18(*b*), where the fundamental frequency and higher harmonics are clearly captured. Although the measurements made closer to the bluff body have a higher amplitude, the global shedding frequency is indeed the same throughout the entire wake structure. The wavelength is

https://doi.org/10.1017/jfm.2025.10871 Published online by Cambridge University Press

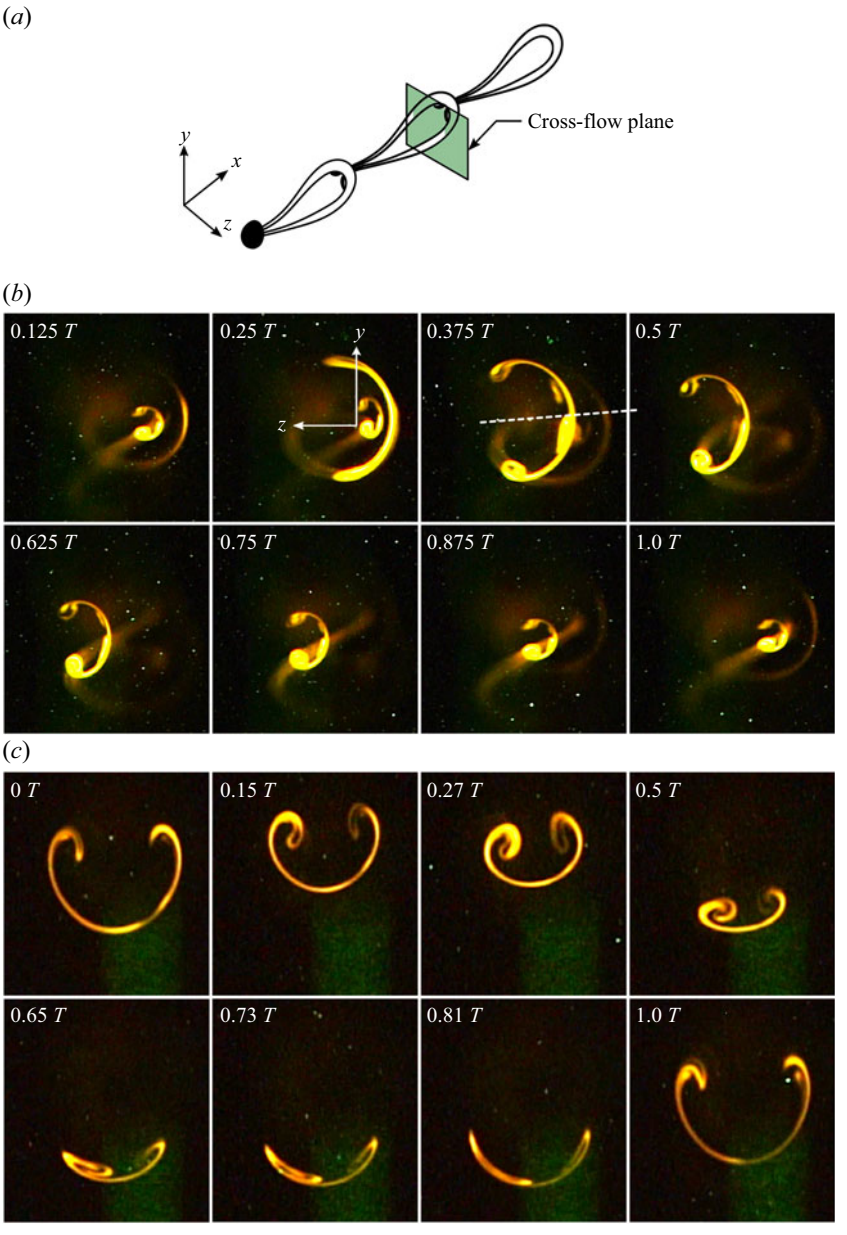


Figure 16. (*a*) Schematic for the visualisations in the cross-flow plane. Cross-flow visualisations using the LIF technique corresponding to the secondary oscillatory bifurcation for aspect ratios $\chi = 0.6$ at $Re \approx 162$ (*b*) and $\chi = 2.0$ at $Re \approx 249$ (*c*). The trailing counter-rotating vortices get connected to each other resulting in the formation of skewed loops. Here, T denotes the time period of one oscillation. The dashed line in (*b*) at $0.375T$ instant indicates the plane of symmetry.

obtained by calculating the average distance between the observed crests and troughs in the spatially well-developed region further downstream of the bluff body. The variations of the Strouhal number and the wavenumber as a function of the aspect ratio are shown in figures 19(*a*) and 19(*b*), respectively. The values from experimental measurements, made at three different aspect ratios, are shown alongside the numerically obtained values from

https://doi.org/10.1017/jfm.2025.10871 Published online by Cambridge University Press

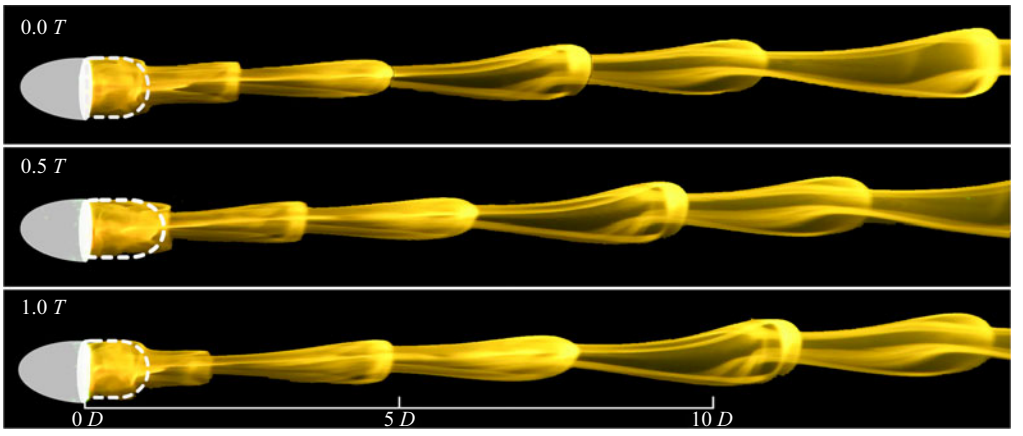


Figure 17. Sequences of LIF visualisations following the secondary oscillatory bifurcation for $\chi = 2$ at $Re \approx 256$. The bubble-shaped bluff body is modelled as an elliptical cap. As observed, the trailing-edge vortices form well-connected loops, retaining a plane of symmetry. The recirculation length is marked in dashed lines $L_R \approx 1.14, 1.41, 1.16$ for the figures from top to bottom. The base flow recirculation length for the same Re is $L_R = 1.79$.

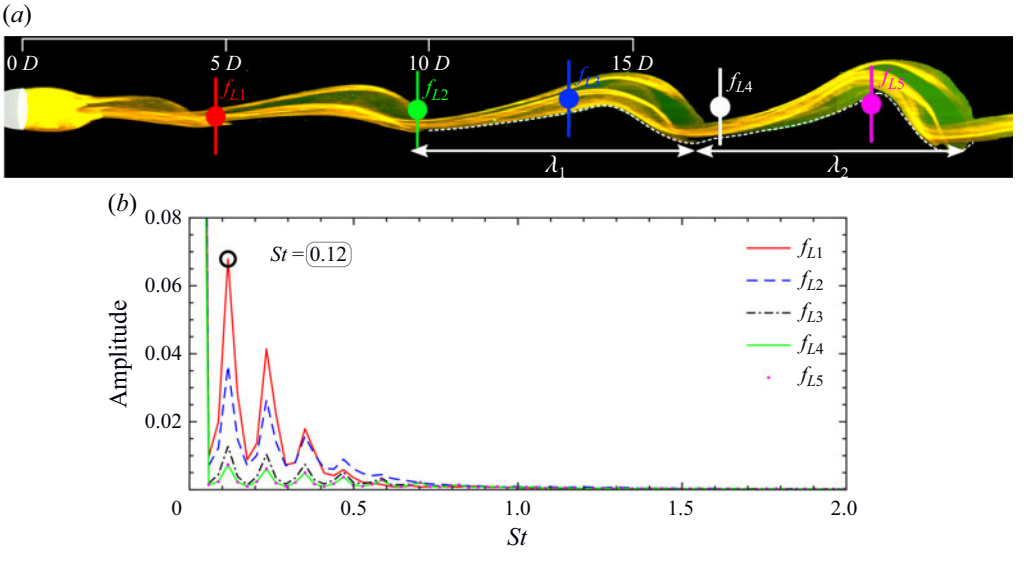


Figure 18. (*a*) The LIF visualisation illustrating the selected locations (f_{L1}, f_{L2}, f_{L3}, f_{L4}, f_{L5}) where image intensity (as a time-series data) were extracted from each frame. The peak-to-peak positions, marked as λ to indicate one wavelength. (*b*) Variation of Strouhal number ($St = fD/U$) at the selected locations for the elliptical cap model with $\chi = 2.0$ at $Re \approx 267$; here f in the Strouhal number expression is the shedding frequency in Hz.

the global stability analysis and these are in good agreement. It is interesting to observe that, although the recirculation lengths L_R and the maximum reversed flow U_{rev} decrease with increasing aspect ratio, the dominant shedding frequency and the wavelength of the fundamental global mode remain constant throughout the entire range of $\chi = 0.2{-}2.0$.

We have carried out the PIV measurements to provide further insight into the flow fields. It should be noted that the PIV acquisition rate is more than four times the dominant shedding frequency. Figure 20 shows the time sequence of the streamwise

https://doi.org/10.1017/jfm.2025.10871 Published online by Cambridge University Press

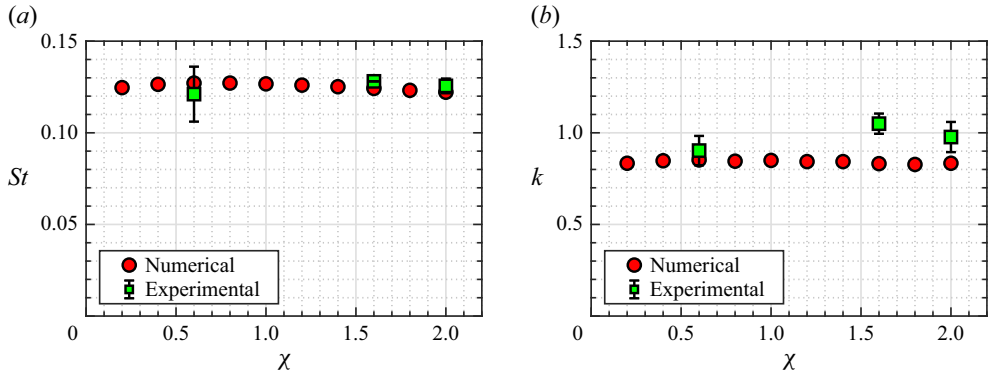


Figure 19. (*a*) Frequency ($St = fD/U$, Strouhal number) and (*b*) Wavenumber ($k = 2\pi/\lambda$) of the leading growth rate for secondary (oscillatory) bifurcation *Re* for different aspect ratios of elliptical model. Experimental details are discussed below.

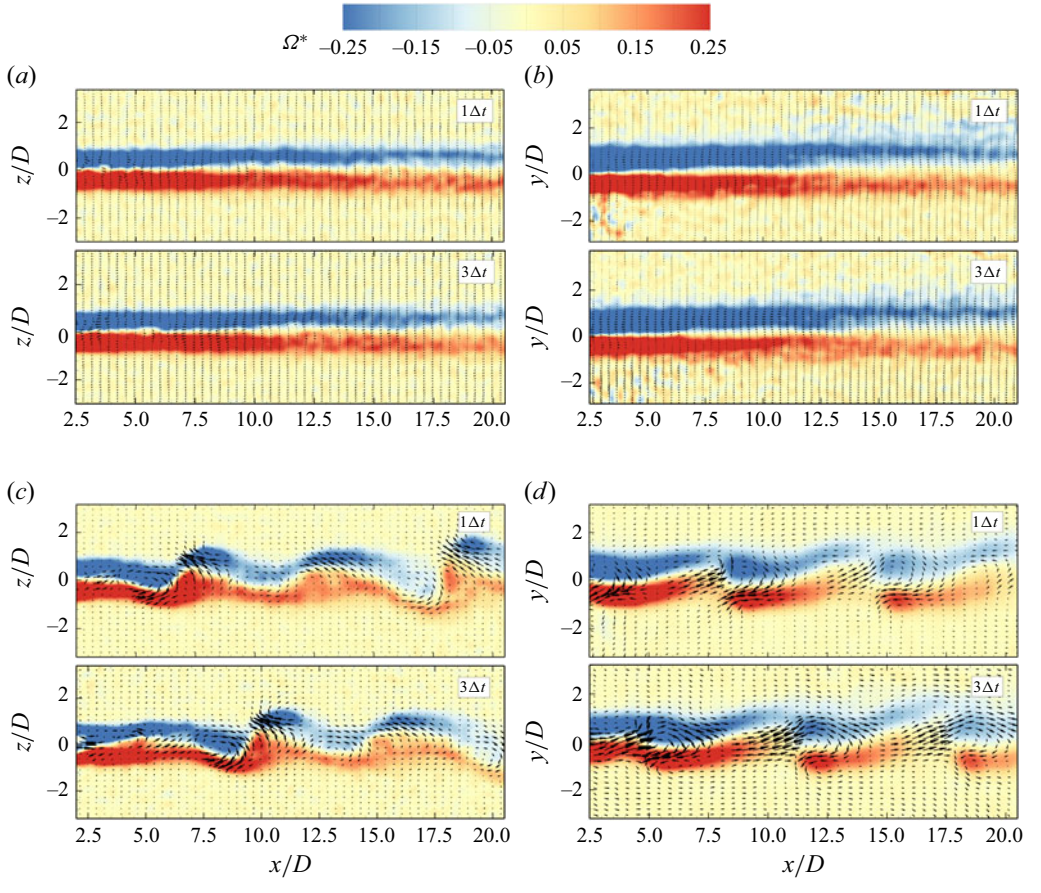


Figure 20. Time sequences of the streamwise vorticity for the primary ($Re \approx 150$) (*a–b*) and secondary ($Re \approx 162$) (*c–d*) bifurcations obtained from PIV measurements of the elliptical cap ($\chi = 0.6$.). The flow direction is from left to right. The contour represents the downstream flow field relative to the model, with the origin located at the centre of the base of the model. The arrows indicate the fluctuating velocity vectors, composed of the fluctuating streamwise velocity, u'_x ($= u_x - \overline{u}_x$) and the fluctuating transverse velocity, u'_y ($= u_y - \overline{u}_y$). These vectors are in relative scale.

https://doi.org/10.1017/jfm.2025.10871 Published online by Cambridge University Press

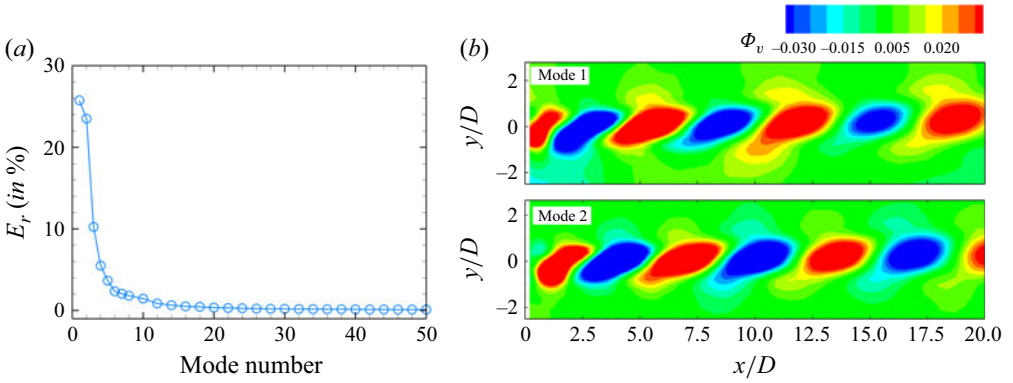


Figure 21. The POD analysis of the cross-stream fluctuating velocity (u'_y) of elliptical shaped model $\chi = 0.6$ at $Re \approx 178$. (*a*) Relative energy (in %) vs POD mode; (*b*) POD mode 1 and mode 2.

vorticity ($\omega_z = \partial_x u_y - \partial_y u_x$) in the x–z and x–y planes, which correspond to the top and side views, for $\chi = 0.6$. The spatial distributions corresponding to the primary stationary bifurcation are shown in figures 20(*a*) and 20(*b*), for the top and side views, respectively, and those corresponding to the secondary oscillatory bifurcation in figures 20(*c*) and 20(*d*), respectively. The time sequence of both views clearly shows that the wake is steady after the primary bifurcation, whereas the same is unsteady or oscillatory in nature after the secondary bifurcation. Further, considering the slope in terms of diverging angle of the two threads in figures 14(*a*,*c*) and 20(*a*), we find these values to be approximately 3.1, 2.3 and 2.4 degrees based on the LIF, PIV and DNS data, respectively. Therefore, the flow features that were observed using the LIF technique are correctly captured using the PIV measurements. Although the flow fields are non-axisymmetric, one can clearly deduce the existence of a plane of symmetry (on average over a shedding period) in the wake after the primary and secondary bifurcations, which is consistent with the theoretical predictions reported in the literature (Ghidersa & Dušek 2000; Fabre *et al.* 2008; Meliga *et al.* 2009).

To further our understanding of the wake flow characteristics beyond the secondary bifurcation, we have carried out the POD analysis of the cross-stream fluctuating velocity (u'_y) field obtained from the PIV measurements. Figure 21(*a*) shows the relative energy distribution of the different modes corresponding to $\chi = 0.6$ at $Re \approx 178$. The first two modes are the dominant ones, with the first 10 modes contributing to more than 80 % of the total energy. The spatial distributions of the first two modes are shown in figure 21(*b*). The contour plots clearly reveal the existence of a slight spatial shift between mode 1 and mode 2. Such a spatial shift associated with a pair of near degenerate POD modes is generally observed in the case of bluff-body wakes, and it is often attributed to the existence of the space–time symmetry in the flow (Noack & Eckelmann 1994; Dutta *et al.* 2022). In the present case, the space–time symmetry comes from the periodic vortex shedding behind the model. Figures 15, 17 and 20(*c*–*d*) clearly show the vortex shedding that can be considered as a travelling wave/structure.

Figure 22 shows comparisons of the base flow field with the mean velocity field, and the global mode shape with the POD mode shape obtained from the PIV and DNS data for $\chi = 0.6$. The comparison of the data has been shown only in the x–y plane, as the dominant POD modes were obtained based on the PIV and DNS data in this plane. Figure 22(*a*–*c*) shows the base flow components and the leading global mode. The streamwise velocity component ($\bar{u}_x$) and the radial velocity component ($\bar{u}_r$) show a recirculation region near the separation point. The spatial structure of the global mode shows the coherent nature

https://doi.org/10.1017/jfm.2025.10871 Published online by Cambridge University Press

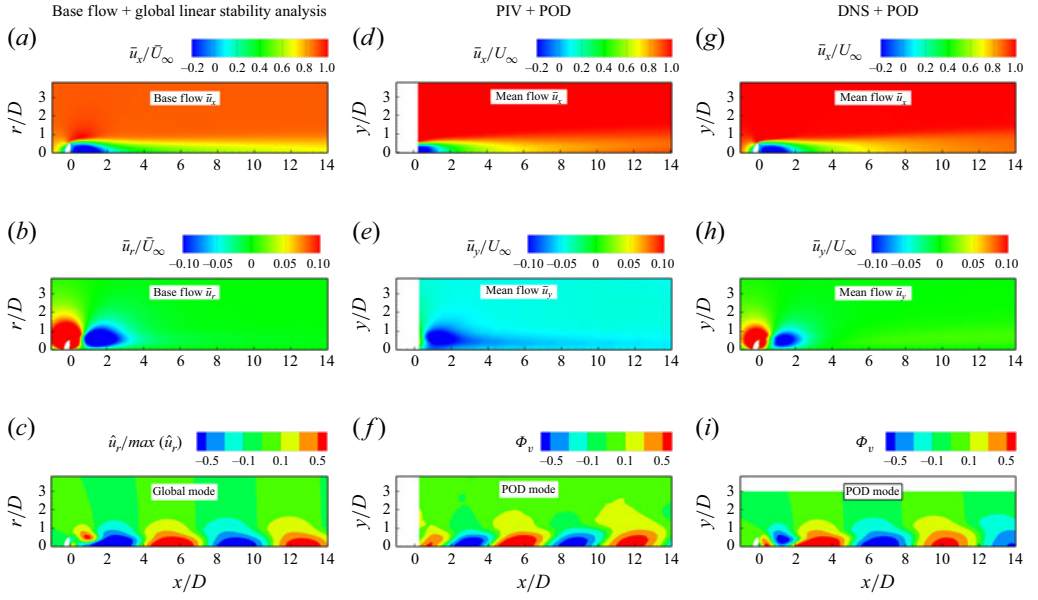


Figure 22. Comparison of global linear stability analysis with POD of experimental and DNS results for $\chi = 0.6$. (*a*) Axial velocity ($\bar{u}_x$) of base flow. (*b*) Radial velocity ($\bar{u}_r$) of base flow. (*c*) The real part of $\hat{u}_r$ leading global mode at $Re = 162$ for azimuthal wavenumber $m = 1$. (*d*) Mean velocity along the *x*-axis ($\overline{u}_x$) and (*e*) mean velocity along the *y*-axis ($\overline{u}_y$) of 600 snapshots. (*f*) First POD mode of u'_y fluctuating velocity for $Re \approx 178$. (*g*) Mean flow velocity $\overline{u}_x$ along the *x*-axis from DNS. (*h*) Mean flow velocity $\overline{u}_x$ in the *y*-axis. (*i*) First POD mode of u'_y fluctuating velocity of DNS for $Re = 178$.

of the flow. The mean flow field and the leading POD mode, obtained from the PIV and DNS data, are shown in figures 22(*d–f*) and 22(*g–i*), respectively. One can see a similarity between the base flow and mean flow fields obtained from the experiments and numerical simulation. The mean flow contours, mainly ($\bar{u}_y$), show slight deviations from the corresponding base flow and DNS data. This may be due to the effect of the model holding device during the PIV acquisition. However, for better comparison, we have extracted the streamwise velocity ($\bar{u}_x$) and the cross-stream velocity ($\bar{u}_y$) components along the centreline of the wake from the PIV and DNS data and plotted in figures 23(*a*) and 23(*b*), respectively. The measured streamwise component quantitively compares well with the DNS data except in the region immediately downstream of the model, which is due to laser reflection from the model and a smaller number of identifiable tracer particles; whereas the cross-stream component shows a systematic deviation. This may be attributed to the fact that the cross-stream component is very small ($\approx 4\,\%$ of U_∞ or $\approx 0.6\,\mathrm{mm\,s^{-1}}$), as compared with the streamwise component, and therefore, its measurement is also very difficult and prone to be noisy even with a 16 MP CCD camera in a larger field of view, as done here for the data shown in figure 22(*d,e*). The cross-stream velocity ($\bar{u}_y$) component measured either with an 8 MP/16 MP CCD camera qualitatively follows a similar trend as in the base flow and DNS data. The global and the POD mode shapes, as can be seen in the last row of this figure, also compare well, at least qualitatively. This similarity is expected as the experimental and the DNS flow fields are close to the secondary bifurcation; to be explicit, the PIV and the DNS data are obtained at $Re = 178$, whereas the global analysis leading to secondary bifurcation has been carried out at $Re = 162$. Overall, the agreement between the global mode based on an axisymmetric base flow and the dominant POD mode extracted from both 2-D PIV and 3-D DNS data in the x–y plane confirms

https://doi.org/10.1017/jfm.2025.10871 Published online by Cambridge University Press

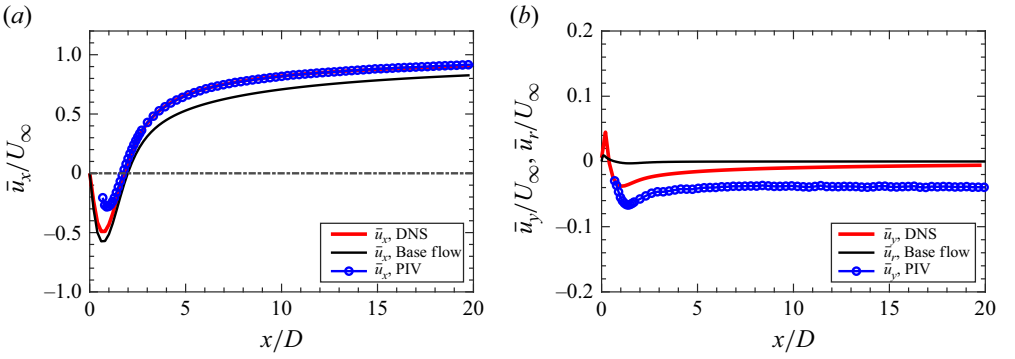


Figure 23. Comparison of mean velocity field obtained from the PIV and DNS data along the centreline, with the base flow field. (*a*) The streamwise velocity component ($\overline{u}_x$). (*b*) The cross-stream velocity component ($\overline{u}_y$).

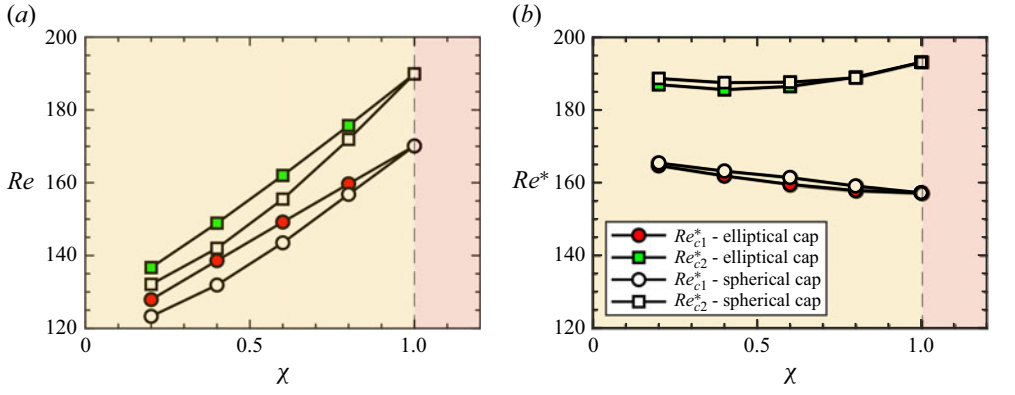


Figure 24. Comparison of critical Reynolds number obtained from the linear stability analysis for the primary (stationary) and secondary (oscillatory) bifurcations of spherical and elliptical cap models with aspect ratios $\chi = 0.2{-}0.4$. Panels show (*a*) Re ($= \rho U D/\mu$) versus χ and (*b*) scaled Re^* ($= \rho|u_{rev}|L_R/\mu$) versus χ.

that the linear instability analysis can describe the underlying flow physics at secondary bifurcation.

4.1. *Effect of geometry*

The effect of modelling the bubble-shaped geometries as elliptical and spherical caps is briefly investigated in this section. As discussed in § 2, these configurations are characterised by a circular base and the height of the bubble, with the bluff bodies modelled as spherical caps being a part of a sphere within the range $0.2 \leqslant \chi \leqslant 1$ (see figure 2). The base flow features from numerical simulations, such as the recirculation length L_R and the maximum reverse-flow velocity U_{rev}, follow similar trends, with the same scaling laws, as observed in the case of elliptical caps (see figure 8). However, subtle differences were observed in the global stability characteristics, which are summarised in figure 24. The spherical cap model exhibits the onset of instability earlier than the elliptical cap model, indicating that the flow behind the elliptical cap is comparatively stable. Notably, both models have the same projected area (normal to the streamwise direction). However, the elliptical model has a curvature that gradually aligns with the streamwise direction, whereas the spherical model has a curvature that does not align as smoothly as the elliptical one. This difference in the edge geometry influences the flow characteristics, as further discussed below by examining the velocity and vorticity distributions near the

https://doi.org/10.1017/jfm.2025.10871 Published online by Cambridge University Press

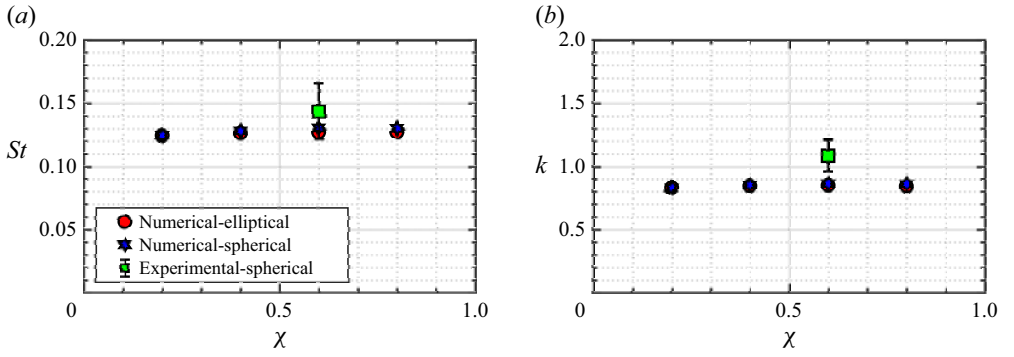


Figure 25. (*a*) Frequency (*St*) and (*b*) wavenumber (k) of the leading growth rate for secondary(oscillatory) bifurcation *Re* for different aspect ratios $\chi = 0.2-0.8$ of elliptical cap and spherical cap.

sharp edge. The critical Reynolds numbers corresponding to spherical caps were found to be lower than the values of elliptical caps, with the differences being larger at lower aspect ratios. Although both models have the same sharp blunt edge at the base (see figure 2*c*, red line curve and blue dashed-line curves), which initiates flow separation, the separation is more pronounced in the spherical cap model as compared with the elliptical cap model due to the sharper curvature. However, the rescaled values of the critical Reynolds numbers, using L_R and U_{rev}, follow the same scaling law for both the configurations, as shown in figure 24(*b*). Furthermore, the differences in Strouhal numbers and the dominant wavenumbers, corresponding to the secondary bifurcation obtained from the global linear stability analysis, are found to be negligible, as shown in figure 25. Additionally, experiments were also carried out at $\chi = 0.6$ for a spherical cap. We found similar flow features (not shown here for brevity) as in the case of an elliptical cap (figure 15). The Strouhal numbers corresponding to spherical and elliptical caps for $\chi = 0.6$ were 0.13, and 0.12, respectively. The Strouhal numbers calculated from experimental observations are 0.14 ± 0.02 for the spherical cap model and 0.12 ± 0.02 for the elliptical cap model. These values are comparatively higher than the Strouhal number predicted by the global linear stability analysis. The discrepancy may be attributed to uncertainties inherent in experimental measurements. Nevertheless, the observed Strouhal numbers fall within the limit of experimental uncertainty and are therefore considered to be in reasonable agreement with the numerical predictions. The spherical cap exhibits a sharper curvature at the separation point, which induces a larger separated wake and a stronger recirculation zone compared with the elliptical cap. This induces earlier vortex shedding and supports higher-frequency wake instabilities. Whereas the elliptical cap has a gradual curvature and a surface more aligned with the streamwise flow, which leads to smoother separation and consequently lower instability frequencies. Furthermore, the spherical cap generates stronger shear layers at the separation edge, which enhances the onset and growth rate of secondary instabilities, as discussed below.

In order to understand the origin of observed differences in the critical Reynolds numbers, especially at lower aspect ratios, we take a closer look at the base flow fields at the downstream edge of the bluff body, prior to flow separation. The variation of the streamwise (axial), $\overline{u}_x$, and the transverse (radial), $\overline{u}_r$, components of the base velocity field, along with the vorticity ($\omega_\theta = \partial_x \overline{u}_r - \partial_r \overline{u}_x$) contours at $\chi = 0.4$ and 0.8 are shown in figure 26 for different Reynolds numbers. We have considered Reynolds numbers that span the primary and secondary bifurcations. One can clearly see the differences in the profiles, which are more pronounced at $\chi = 0.4$, for the streamwise and the transverse

https://doi.org/10.1017/jfm.2025.10871 Published online by Cambridge University Press

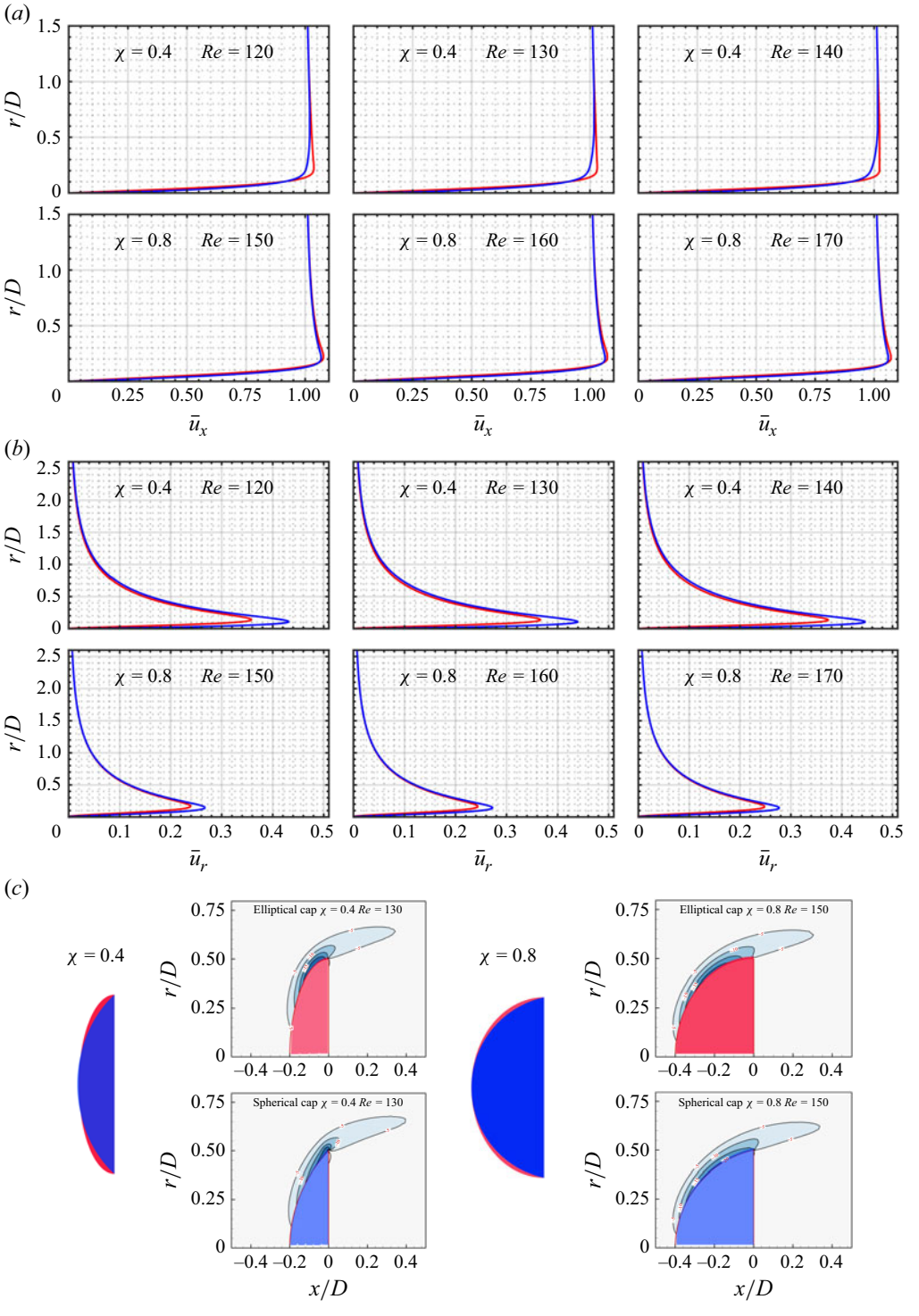


Figure 26. (*a*) Comparison of the streamwise velocity component of the base flow for the elliptical (solid line in red) and spherical cap (solid line in blue) models for $\chi = 0.4$ and $\chi = 0.8$ at different Reynolds numbers. (*b*) Comparison of the transverse velocity component of the base flow for elliptical (solid line in red) and spherical cap (solid line in blue) models for $\chi = 0.4$ and $\chi = 0.8$ at different Reynolds numbers. (*c*) Vorticity ($\omega_\theta = \partial_x \bar{u}_r - \partial_r \bar{u}_x$) contours ($-20 \leqslant \omega_\theta \leqslant 20$) at $\chi = 0.4$ for $Re = 130$ for elliptical and spherical cap models, and at $\chi = 0.8$ for $Re = 150$.

https://doi.org/10.1017/jfm.2025.10871 Published online by Cambridge University Press

velocity components in figures 26(*a*) and 26(*b*), respectively. Specifically, the maximum value of $\overline{u}_x$ is larger in the boundary layer region at the downstream edge ($0 \leqslant r/D \leqslant 0.5$) for the case of elliptical cap. On the other hand, the radial velocity component, $\overline{u}_r$, is found to be larger for the case of spherical cap. This difference may be attributed to the variation in the surface curvature between the two geometries. The curved surface of the elliptical cap is more aligned with the streamwise direction, resulting in a smoother axial velocity distribution. In contrast, the spherical cap induces stronger radial effects due to its steeper curvature. This behaviour is further examined by analysing the vorticity, which incorporates both axial and radial velocity gradients. The vorticity contours with iso-lines ranging from –20 to 0, as shown in figure 26(*c*), exhibit stronger and more localised vorticity near the separation region; this can be deduced from the tighter spacing of the iso-lines. In contrast, the elliptical cap shows a broader distribution of vorticity, indicating a more diffused shear layer (e.g. the iso-line, $\omega_\theta = -20$, is more distributed downstream in the elliptical case). Since the transverse velocity is stronger and the streamwise velocity is weaker, it is highly plausible that the stronger shear layer for the spherical cap model is more prone to being affected by the transverse velocity, leading to an earlier roll-up of the shear layer and a lower critical Reynolds number. This explains why the wakes of spherical caps become unstable at an earlier Reynolds number than elliptical caps.

5. Concluding remarks

The stability and dynamics of flows past axisymmetric bluff bodies, motivated by the shapes of bubbles rising in quiescent fluids, have been investigated both numerically and experimentally. The bubble-shaped bluff bodies were modelled as spherical and as elliptical caps, with a circular base of diameter D, and by the height (or width) of the bubble W. The geometries are characterised by the aspect ratio $\chi = W/(D/2)$, which is varied within the range $0.2 \leqslant \chi \leqslant 1$ for the spherical cap, and $0.2 \leqslant \chi \leqslant 2$ for the elliptical cap. The recirculation length L_R, which is one of the measures of the spatial extent of the absolutely unstable region, and the maximum reverse-flow velocity U_{rev}, which is a measure of the growth of disturbances that travel upstream, in the wake of the bluff bodies were found to decrease with increasing aspect ratio. Global linear stability analyses were carried out on axisymmetric base flow fields subject to 3-D perturbations. As observed in earlier studies on bluff-body wakes, the primary bifurcation is stationary, followed by an oscillatory secondary bifurcation, with the leading global mode corresponding to azimuthal wavenumber $m = 1$. The critical Reynolds numbers were found to increase linearly with increasing aspect ratio. Furthermore, the critical Reynolds number corresponding to primary bifurcation is found to be independent of the aspect ratio when re-scaled using L_R and U_{rev} as the length and velocity scales, respectively.

The wake flow characteristics were examined experimentally using the LIF and the PIV techniques. The LIF visualisations have shown that at the primary bifurcation the wake is characterised by two trailing counter-rotating vortices resulting in a stationary two-threaded bifid structure. As the Reynolds number is increased further, the vortices get connected to each other, resulting in the formation of strongly skewed loops which get convected downstream. These observations have also been confirmed using the 3-D DNS. Interestingly, cross-flow visualisations have revealed that the flow has a planar symmetry following the primary bifurcation, which is retained beyond the secondary bifurcation. The measured wavelengths and frequencies, and the critical Reynolds numbers obtained from experimental and DNS data are in good agreement with the values obtained using linear stability analyses performed on axisymmetric base flow fields. Furthermore, the

https://doi.org/10.1017/jfm.2025.10871 Published online by Cambridge University Press

POD analysis of the fluctuating cross-stream velocity obtained from the PIV and DNS data is found to be consistent with the global mode shape. The insights gained from the present study can be used for designing efficient control strategies of bluff-body wakes.

Acknowledgements. We gratefully acknowledge the use of the PARAM Sanganak high-performance computing facility. We extend our sincere thanks to Professor K. Poddar and the National Wind Tunnel Facility (NWTF) for providing the laser and camera used in the PIV experiments. We also thank Mr Vivek M., Mr H. Om, Mr Dorilal and Mr A. Yadav for their help with the experimental set-up.

Funding. The authors thank the partial financial support from the Aeronautics Research & Development Board (Grant Numbers ARDB/01/1031875/M/I and ARDB/01/1031880/M/I) and Indian Institute of Technology Kanpur (Grant Number IITK/ME/2022358).

Declaration of interests. The authors report no conflict of interest.

References

Aniffa, S.M., Caesar, V.S., Dabaria, V. & Mandal, A.C. 2023 Characteristics of geometry-and pressure-induced laminar separation bubbles at an enhanced level of free-stream turbulence. *J. Fluid Mech.* **957**, A19.

Balamurugan, G. & Mandal, A.C. 2017 Experiments on localized secondary instability in bypass boundary layer transition. *J. Fluid Mech.* **817**, 217–263.

Berkooz, G., Holmes, P. & Lumley, J.L. 1993 The proper orthogonal decomposition in the analysis of turbulent flows. *Annu. Rev. Fluid Mech.* **25** (1), 539–575.

Bhattacharyya, S., Khan, I.H., Verma, S., Kumar, S. & Poddar, K. 2022 Experimental investigation of three-dimensional modes in the wake of a rotationally oscillating cylinder. *J. Fluid Mech.* **950**, A10.

Bobinski, T., Goujon-Durand, S. & Wesfreid, J.E. 2014 Instabilities in the wake of a circular disk. *Phys. Rev. E* **89** (5), 053021.

Bohorquez, P., Sanmiguel-Rojas, E., Sevilla, A., Jiménez-González, J.I. & Martínez-Bazán, C. 2011 Stability and dynamics of the laminar wake past a slender blunt-based axisymmetric body. *J. Fluid Mech.* **676**, 110–144.

Bonnefis, P., Sierra-Ausin, J., Fabre, D. & Magnaudet, J. 2024 Path instability of deformable bubbles rising in Newtonian liquids: a linear study. *J. Fluid Mech.* **980**, A19.

Cano-Lozano, J.C., Tchoufag, J., Magnaudet, J. & Martínez-Bazán, C. 2016 A global stability approach to wake and path instabilities of nearly oblate spheroidal rising bubbles. *Phys. Fluids* **28** (1), 014102.

Chiarini, A., Quadrio, M. & Auteri, F. 2022 A new scaling for the flow instability past symmetric bluff bodies. *J. Fluid Mech.* **936**, R2.

Chomaz, J.-M. 2005 Global instabilities in spatially developing flows: non-normality and nonlinearity. *Annu. Rev. Fluid Mech.* **37**, 357–392.

Chrust, M., Bouchet, G. & Dušek, J.A.N. 2010 Parametric study of the transition in the wake of oblate spheroids and flat cylinders. *J. Fluid Mech.* **665**, 199–208.

Constantinescu, G. & Squires, K. 2000 LES and DES investigations of turbulent flow over a sphere. In *38th Aerospace Sciences Meeting and Exhibit*, pp. 540. American Institute of Aeronautics and Astronautics.

Dutta, D., Kanshana, I., Gopalakrishnan, S.S. & Mandal, A.C. 2022 Experimental studies on the frequency selection in flat plate wakes: mean-flow stability analyses and low-dimensional modeling. *Phys. Rev. Fluids* **7** (4), 044102.

Ellingsen, K. & Risso, F. 2001 On the rise of an ellipsoidal bubble in water: oscillatory paths and liquid-induced velocity. *J. Fluid Mech.* **440**, 235–268.

Ern, P., Risso, F., Fabre, D. & Magnaudet, J. 2012 Wake-induced oscillatory paths of bodies freely rising or falling in fluids. *Annu. Rev. Fluid Mech.* **44** (1), 97–121.

Fabre, D., Auguste, F. & Magnaudet, J. 2008 Bifurcations and symmetry breaking in the wake of axisymmetric bodies. *Phys. Fluids* **20** (5), 051702.

Fernandes, P.C., Risso, F., Ern, P. & Magnaudet, J. 2007 Oscillatory motion and wake instability of freely rising axisymmetric bodies. *J. Fluid Mech.* **573**, 479–502.

Ghidersa, B. & Dušek, J.A.N. 2000 Breaking of axisymmetry and onset of unsteadiness in the wake of a sphere. *J. Fluid Mech.* **423**, 33–69.

Gopalakrishnan, S.S. 2014 *Dynamics and stability of flow through abdominal aortic aneurysms. Theses,* Université Claude Bernard.

https://doi.org/10.1017/jfm.2025.10871 Published online by Cambridge University Press

GOPALAKRISHNAN, S.S., PIER, B. & BIESHEUVEL, A. 2014 Global stability analysis of flow through a fusiform aneurysm: steady flows. *J. Fluid Mech.* **752**, 90–106.

GUMOWSKI, K., MIEDZIK, J., GOUJON-DURAND, S., JENFFER, P. & WESFREID, J.E. 2008 Transition to a time-dependent state of fluid flow in the wake of a sphere. *Phys. Rev. E* **77** (5), 055308.

HAMMOND, D.A. & REDEKOPP, L.G. 1997 Global dynamics of symmetric and asymmetric wakes. *J. Fluid Mech.* **331**, 231–260.

JEONG, J. & HUSSAIN, F. 1995 On the identification of a vortex. *J. Fluid Mech.* **285**, 69–94.

JIMÉNEZ-GONZÁLEZ, J.I., MANGLANO-VILLAMARÍN, C. & COENEN, W. 2019 The role of geometry on the global instability of wakes behind streamwise rotating axisymmetric bodies. *Eur. J. Mech.-B/Fluids* **76**, 205–222.

JOHNSON, T.A. & PATEL, V.C. 1999 Flow past a sphere up to a Reynolds number of 300. *J. Fluid Mech.* **378**, 19–70.

KHAN, I.H., SUNIL, P., BHATTACHARYYA, S., YADAV, R., PODDAR, K. & KUMAR, S. 2023 Flow past two rotationally oscillating cylinders. *J. Fluid Mech.* **969**, A16.

KHAN, M.H., KHAN, H.H., SHARMA, A. & AGRAWAL, A. 2020 Laminar vortex shedding in the wake of a cube. *J. Fluids Engng* **142** (11), 111301.

KIM, D. & CHOI, H. 2002 Laminar flow past a sphere rotating in the streamwise direction. *J. Fluid Mech.* **461**, 365–386.

KIM, D. & CHOI, H. 2003 Laminar flow past a hemisphere. *Phys. Fluids* **15** (8), 2457–2460.

LANDAU, L.D. 1944 On the problem of turbulence. *Dokl. Akad. Nauk USSR* **44**, 311.

MAGARVEY, R.H. & BISHOP, R.L. 1961*a* Transition ranges for three-dimensional wakes. *Can. J. Phys.* **39** (10), 1418–1422.

MAGARVEY, R.H. & BISHOP, R.L. 1961*b* Wakes in liquid-liquid systems. *Phys. Fluids* **4** (7), 800–805.

MAGARVEY, R.H. & MACLATCHY, C.S. 1965 Vortices in sphere wakes. *Can. J. Phys.* **43** (9), 1649–1656.

MAGNAUDET, J. & MOUGIN, G. 2007 Wake instability of a fixed spheroidal bubble. *J. Fluid Mech.* **572**, 311–337.

MANDAL, A.C., VENKATAKRISHNAN, L. & DEY, J. 2010 A study on boundary-layer transition induced by free-stream turbulence. *J. Fluid Mech.* **660**, 114–146.

MARQUET, O., SIPP, D. & JACQUIN, L. 2008 Sensitivity analysis and passive control of cylinder flow. *J. Fluid Mech.* **615**, 221–252.

MELIGA, P., CHOMAZ, J.-M. & SIPP, D. 2009 Unsteadiness in the wake of disks and spheres: instability, receptivity and control using direct and adjoint global stability analyses. *J. Fluids Struct.* **25** (4), 601–616.

MITTAL, R. 1999 A Fourier–Chebyshev spectral collocation method for simulating flow past spheres and spheroids. *Intl J. Numer. Meth. Fluids* **30** (7), 921–937.

MONKEWITZ, P.A. 1988 A note on vortex shedding from axisymmetric bluff bodies. *J. Fluid Mech.* **192**, 561–575.

MOUGIN, G. & MAGNAUDET, J. 2001 Path instability of a rising bubble. *Phys. Rev. Lett.* **88** (1), 014502.

MUNIYAMMAL, R., MANDAL, A.C. & KUMAR, S. 2020 V0036: Dynamics of a rising air bubble through a liquid-liquid interface. In *73th Annual Meeting of the APS Division of Fluid Dynamics*. American Physical Society.

NAKAMURA, I. 1976 Steady wake behind a sphere. *Phys. Fluids* **19** (1), 5–8.

NATARAJAN, R. & ACRIVOS, A. 1993 The instability of the steady flow past spheres and disks. *J. Fluid Mech.* **254**, 323–344.

NOACK, B.R. & ECKELMANN, H. 1994 A global stability analysis of the steady and periodic cylinder wake. *J. Fluid Mech.* **270**, 297–330.

ORMIÈRES, D. & PROVANSAL, M. 1999 Transition to turbulence in the wake of a sphere. *Phys. Rev. Lett.* **83** (1), 80.

PIER, B. 2008 Local and global instabilities in the wake of a sphere. *J. Fluid Mech.* **603**, 39–61.

PROVANSAL, M., MATHIS, C. & BOYER, L. 1987 Bénard-von Kármán instability: transient and forced regimes. *J. Fluid Mech.* **182**, 1–22.

PROVANSAL, M., SCHOUVEILER, L. & LEWEKE, T. 2004 From the double vortex street behind a cylinder to the wake of a sphere. *Eur. J. Mech.-B/Fluids* **23** (1), 65–80.

ROOS, F.W. & WILLMARTH, W.W. 1971 Some experimental results on sphere and disk drag. *AIAA J.* **9** (2), 285–291.

SAHA, A.K. 2004 Three-dimensional numerical simulations of the transition of flow past a cube. *Phys. Fluids* **16** (5), 1630–1646.

SANMIGUEL-ROJAS, E., JIMÉNEZ-GONZÁLEZ, J.I., BOHORQUEZ, P., PAWLAK, G. & MARTÍNEZ-BAZÁN, C. 2011 Effect of base cavities on the stability of the wake behind slender blunt-based axisymmetric bodies. *Phys. Fluids* **23** (11), 114103.

https://doi.org/10.1017/jfm.2025.10871 Published online by Cambridge University Press

SANMIGUEL-ROJAS, E., SEVILLA, A., MARTÍNEZ-BAZÁN, C. & CHOMAZ, J.-M. 2009 Global mode analysis of axisymmetric bluff-body wakes: stabilization by base bleed. *Phys. Fluids* **21** (11), 114102.

SARKAR, S. & DE, A.K. 2025 Vortex-induced vibration of a streamwise and transversely rotating sphere. *J. Fluid Mech.* **1016**, A18.

SCHOUVEILER, L. & PROVANSAL, M. 2002 Self-sustained oscillations in the wake of a sphere. *Phys. Fluids* **14** (11), 3846–3854.

SHENOY, A.R. & KLEINSTREUER, C. 2008 Flow over a thin circular disk at low to moderate Reynolds numbers. *J. Fluid Mech.* **605**, 253–262.

SIROVICH, L. 1987 Turbulence and the dynamics of coherent structures. I. Coherent structures. *Q. Appl. Maths* **45** (3), 561–571.

SREENIVASAN, K.R., STRYKOWSKI, P.J. & OLINGER, D.J. 1987 Hopf bifurcation, landau equation, and vortex shedding behind circular cylinders. In *Forum On Unsteady Flow Separation*, vol. 1, pp. 1–13. ASME New York.

SUNIL, P., KUMAR, S. & PODDAR, K. 2022 Flow past a rotationally oscillating cylinder with an attached flexible filament. *J. Fluid Mech.* **930**, A3.

SZALTYS, P., CHRUST, M., PRZADKA, A., GOUJON-DURAND, S., TUCKERMAN, L.S. & WESFREID, J.E. 2012 Nonlinear evolution of instabilities behind spheres and disks. *J. Fluids Struct.* **28**, 483–487.

TANEDA, S. 1956 Experimental investigation of the wake behind a sphere at low reynolds numbers. *J. Phys. Soc. Japan* **11** (10), 1104–1108.

THOMPSON, M.C., LEWEKE, T. & PROVANSAL, M. 2001 Kinematics and dynamics of sphere wake transition. *J. Fluids Struct.* **15** (3–4), 575–585.

ZHENG, X.-L., PAN, J.-H. & NI, M.-J. 2023 Linear global stability of a flow past a sphere under a streamwise magnetic field. *J. Fluid Mech.* **970**, A16.

https://doi.org/10.1017/jfm.2025.10871 Published online by Cambridge University Press